

Fundamental Trade-offs in Quantized Hybrid Radar Fusion: A CRB-Rate Perspective

Akhileswar Chowdary, *Student Member, IEEE*, Ahmad Bazzi, and Marwa Chafii, *Senior Member, IEEE*

Abstract—While recent advancements have highlighted the role of low-resolution analog-to-digital converters (ADCs) in integrated sensing and communication (ISAC) systems, the specific impact of ADC resolution on hybrid radar fusion (HRF) remains relatively unexplored. The uplink (UL) paths in HRF, comprising both direct and reflected signals within the same frequency band, pose unique challenges, particularly given that the reflected signal is often significantly weaker than the direct path, making HRF systems susceptible to ADC resolution. To investigate the influence of quantization and ADC resolution on HRF, we employ the quantized Cramér-Rao bound (CRB) as a metric for sensing accuracy. This work derives the quantized CRB specifically for HRF systems and the quantized communication rate. We extend our analysis to obtain lower bounds on the Fisher Information Matrix (FIM) and UL communication rates, which we use to characterize quantized HRF systems. Using these derived bounds, we analyze quantized HRF systems through the lens of CRB-rate boundaries. We obtain the CRB-rate boundary through two optimization problems, where each solution point represents a trade-off boundary between the sensing accuracy and the communication rate. Extensive simulations illustrate the influence of ADC resolution, DR, and various system parameters on the CRB-rate boundary of HRF systems. These results offer critical insights into the design of efficient and high-performance HRF systems.

Index Terms—Integrated sensing and communications (ISAC), analog-to-digital converters (ADCs), CRB-rate tradeoff, dual-functional radar communication (DFRC), and hybrid radar fusion (HRF).

I. INTRODUCTION

RAPID advancements in wireless communications technologies, spanning from 2G to 5G, have profoundly shaped the modern era, enabling a variety of applications such as intelligent transportation systems, localization, remote healthcare, unmanned aerial vehicle (UAV) networks, digital twins, smart homes, and smart cities. These emerging applications require seamless communication and sensing capabilities integration to function effectively [1]. Consequently, the need for integrated sensing and communication (ISAC) has naturally arisen in these domains. Recognizing the critical importance of ISAC for future applications, the International Telecommunication Union (ITU) has designated it as one of the six critical use cases for 6G [2]. ISAC is now poised to become a fundamental feature of 6G, attracting significant interest from academia [3] and industry. DFRC systems achieve integration by sharing common hardware, spectrum,

waveform [4], and signal processing techniques between radar and communication functionalities, resulting in reduced hardware costs, lower energy consumption, and improved spectral efficiency [5], [6].

Despite these advancements, the increasing sophistication of wireless systems comes at a cost, particularly in terms of higher power consumption, security leakage [7], increased complexity, and the need for advanced hardware. The deployment of 5G in the millimeter-wave (mmWave) bands and the ongoing exploration of sub-THz frequencies have driven many studies on ISAC systems to focus on these higher frequency ranges. However, operating at mmWave and sub-THz frequencies significantly increases both hardware costs and power consumption, particularly for high-resolution analog-to-digital converters (ADCs) [8], [9]. Specifically, the power consumption of an ADC is proportional to $2^b \cdot f_s$, where b is the resolution of the ADC and f_s is the sampling rate [10]. To mitigate hardware costs and power consumption, a promising approach is to utilize low-resolution ADCs.

Recent research has begun to address the usage of low-resolution ADCs in ISAC systems. In [11], the authors considered a scenario in which a DFRC BS transmits communication symbols to multiple single-antenna users while probing the environment to detect and track targets. The authors assume that the BS transmitter is equipped with one-bit digital-to-analog converters (DACs) and infinite-resolution ADCs at the receiver. The study focuses on designing transmit sequences that minimize the communication symbols' mean squared error (MSE) while satisfying a Cramér-Rao bound (CRB) for sensing accuracy. Similarly, [12] explores the application of rate-splitting multiple access (RSMA) for ISAC systems using low-resolution digital-to-analog converters (DACs). The paper proposes an optimization framework that takes into account both radar beam patterns and the distortion introduced by the DACs while adhering to a total transmit power constraint. Meanwhile, [13] introduces a quantizer design for ISAC-MIMO systems with pre-processing and post-processing matrices optimized to minimize the MSE of the target's impulse response.

Further contributions include [14], which examines a MIMO-DFRC system equipped with one-bit ADCs and proposes joint analog and digital processing design to enhance target parameter estimation. Additionally, [15] examines a DFRC system that transmits radar and communication signals to a remote bit-constrained receiver. The study designs a hybrid analog/digital receiver to reduce the impact of quantization distortion. In [16], the authors propose a multiple beam strategy to maximize the received signal power in an ISAC

Akhileswar Chowdary is with the NYU WIRELESS, NYU Tandon School of Engineering, New York University (NYU), Brooklyn, NY 11201 USA (email: akhileswar.chowdary@nyu.edu).

Ahmad Bazzi and Marwa Chafii are with the Engineering Division, New York University (NYU) Abu Dhabi, Abu Dhabi, United Arab Emirates, and the NYU WIRELESS, NYU Tandon School of Engineering, Brooklyn, NY 11201 USA (e-mail: ahmad.bazzi@nyu.edu; marwa.chafii@nyu.edu).

mmWave MIMO system, leveraging the quantization of the beamforming vector using two phase shifters. Works, such as [17], propose energy-efficient signal detection schemes for low-precision quantization, showing performance gains over linear minimum mean square error (LMMSE)-based methods.

Recent efforts, such as [18], have focused on transmit waveform design to minimize MSE between designed and desired beam patterns, considering low-resolution DACs and communication quality of service (QoS) constraints. In [19], the authors develop a CRB optimization framework that jointly designs the transmit precoding and reconfigurable intelligent surface (RIS) configuration, while ensuring that signal-to-interference-plus-noise ratio (SINR) constraints are met. Meanwhile, [20] focuses on discrete RIS reflection coefficient design for ISAC, aiming to minimize multi-user interference under CRB constraints. Several additional studies, such as [21]–[23], highlight the effectiveness of using low-resolution ADCs in mmWave ISAC systems. These works propose different algorithms to minimize the performance loss caused by quantization.

While recent research has begun to explore the role of low-resolution ADCs in ISAC systems, the specific effects of ADC resolution on hybrid radar fusion (HRF) [24] remain underexplored. In HRF, a unique challenge arises due to the presence of two uplink (UL) links from the user: the direct path and the reflected signal from the target, both operating in the same frequency band. In specific scenarios, the reflected signal’s power may be significantly lower than the direct path’s. Differentiating between these two paths under such conditions often requires high-resolution ADCs. Therefore, understanding how the ADC resolution affects the ability to distinguish between these paths is critical for HRF systems. Moreover, the algorithms and techniques discussed in the existing literature cannot be directly applied to HRF due to the substantial differences in system models and the lack of studies addressing the dynamic range (DR) of ADCs required for HRF. In this paper, we investigate the effects of ADC resolution on HRF, focusing on how the required resolution changes based on the power disparity between direct and reflected paths. By studying this relationship, we aim to provide insights into the appropriate ADC resolution required for HRF systems under varying power conditions, ultimately balancing performance with hardware efficiency and the necessary DR. The main contributions of this work are as follows.

- **Derivation of quantized CRB and performance bounds for HRF systems.** We rigorously derive the quantized CRB, the measure of sensing performance in ISAC, for the HRF system, incorporating the effects of finite-resolution ADCs. Through this derivation, we demonstrate the effect of stochastic resonance within the HRF framework and validate the accuracy of the derived CRB through simulations. Additionally, leveraging the Bussgang theorem, we derive a lower bound on the FIM, corresponding to an upper bound on the CRB. Furthermore, we establish a lower bound on the UL rate, a measure of the communication performance in ISAC, using the Bussgang theorem. We use these bounds to demonstrate the effect of the DR of the ADC and

quantization on the limits of the HRF system.

- **Optimization problems for CRB-UL rate boundary characterization.** Building on the derived lower bounds for both the FIM and UL rates, we formulate two optimization problems. These problems are designed to characterize the quantized CRB-rate boundary of the HRF system under specified conditions. The solutions to these optimization problems yield optimal precoding strategies for both the BS and the communication users. Consequently, the CRB-rate boundaries derived from these optimal precoders underscore the inherent performance trade-offs in the quantized HRF system. This approach allows us to investigate the impact of ADC resolution and DR on the HRF system through the lens of these quantized CRB-rate boundaries.
- **Extensive simulation results.** Through comprehensive simulations, we investigate how the ADC DR and resolution affect the performance of the HRF system. Additionally, we demonstrate the impact of ADC resolution on the system’s sensing capabilities. Our results provide insights into how various system parameters influence the CRB and communication rate, as illustrated through the CRB-rate boundary, shedding light on both the advantages and limitations of HRF systems.

The motivation for examining the impact of ADC resolution and DR through CRB-rate boundaries is to evaluate the effects of ADC DR on HRF systems jointly and to explore CRB-rate trade-offs rather than addressing them separately. While existing studies focus on CRB-DL rate trade-offs, *this work uniquely addresses the CRB-UL rate trade-off specific to HRF systems. Notably, this research is the first to explore the impacts of ADC DR and quantization on HRF* and pioneers the investigation of sensing-communication trade-offs in quantized HRF systems. This work establishes a foundation for future research on CRB-rate boundaries amid hardware impairments and advances strategies to mitigate these effects.

Notations: Lowercase boldface denotes vectors, uppercase boldface denotes matrices, and normal font represents scalars. $(\cdot)^T$, $(\cdot)^H$, and $(\cdot)^*$ represent transpose, Hermitian, and conjugate, respectively. $\text{tr}(\cdot)$ and $|\cdot|$ indicate the trace and determinant of a matrix. For a square matrix \mathbf{A} , $\mathbf{A} \succeq 0$ and $\mathbf{A} \succ 0$ denote that \mathbf{A} is positive semidefinite and positive definite. $\text{diag}(\cdot)$ creates a diagonal matrix with the argument’s diagonal elements. $\mathbb{R}^{x \times y}$ and $\mathbb{C}^{x \times y}$ represent real and complex matrices of dimension $x \times y$. $\mathbb{E}\{\cdot\}$ or $\mathbb{E}[\cdot]$ indicate statistical expectation, and $\Re(\cdot)$ and $\Im(\cdot)$ are the real and imaginary parts. The ℓ_2 norm is denoted by $\|\cdot\|$, and $|z|$ represents the magnitude of z . The imaginary unit is $j = \sqrt{-1}$.

II. SYSTEM MODEL

Fig. 1 illustrates the HRF with a DFRC BS, K communication users whose set is defined as $\mathcal{K} \in \{1, \dots, K\}$, and P targets in the scene. The DFRC BS is equipped with N transmit and receive antennas. Additionally, there are P targets in the scene, where the i^{th} target is present at an angle of θ_i^{tar} to the DFRC BS. The set of angles of arrival (AoAs) of all the P targets is denoted as $\Theta^{\text{tar}} = \{\theta_1^{\text{tar}}, \dots, \theta_P^{\text{tar}}\}$. In the DL,

the ℓ^{th} OFDM symbol is given as

$$\mathbf{s}_{\ell,0}(t) = \left(\sum_{m \in \mathcal{C}_0} b_{m,0}^{(\ell)} e^{(j2\pi m \Delta_f t)} \Pi(t - \ell T) \right) \mathbf{f}, \quad (1)$$

where $\mathbf{s}_{\ell,0}(t) \in \mathbb{C}^{N \times 1}$, \mathcal{C}_0 is the set of subcarriers allocated to the DL, $b_{m,0}^{(\ell)}$ is the data symbol modulating m^{th} subcarrier in ℓ^{th} OFDM symbol duration, Δ_f is the subcarrier spacing, $\Pi(t)$ is a windowing function, $T = 1/\Delta_f$ is the symbol duration, and $\mathbf{f} \in \mathbb{C}^{N \times 1}$ is the precoding vector. Similarly, the ℓ^{th} OFDM symbol transmitted by the k^{th} user with N_k^{u} antennas in the UL can be expressed as [24]

$$\mathbf{s}_{\ell,k}(t) = \left(\sum_{m \in \mathcal{C}_k} b_{m,k}^{(\ell)} e^{(j2\pi m \Delta_f t)} \Pi(t - \ell T) \right) \mathbf{f}_k^{\text{u}}, \quad (2)$$

where $\mathbf{s}_{\ell,k}(t) \in \mathbb{C}^{N_k^{\text{u}} \times 1}$, \mathcal{C}_k is the set of subcarriers allocated to the k^{th} user, $b_{m,k}^{(\ell)}$ is the data symbol from k^{th} user modulating m^{th} subcarrier, and $\mathbf{f}_k^{\text{u}} \in \mathbb{C}^{N_k^{\text{u}} \times 1}$ is the precoding vector. All the symbols are upconverted to the center frequency f_c before transmission. The received and down-converted signal at the DFRC BS is $\mathbf{r}_{\ell}(t) = \mathbf{r}_{\ell}^{\text{echo}}(t) + \sum_{k=1}^K \mathbf{r}_{\ell,k}^{\text{UL}}(t) + \mathbf{z}_{\ell}(t)$, where $\mathbf{r}_{\ell}^{\text{echo}}(t)$ is the echo received at time t , $\mathbf{r}_{\ell,k}^{\text{UL}}(t)$ is the received signal due to the UL signal transmitted by the k^{th} user, and $\mathbf{z}_{\ell}(t)$ is additive white Gaussian noise (AWGN) with mean 0 and variance σ^2 . $\mathbf{r}_{\ell}^{\text{echo}}(t)$ and $\mathbf{r}_{\ell,k}^{\text{UL}}(t)$ are given as follows

$$\mathbf{r}_{\ell}^{\text{echo}}(t) = \sum_{i \in \Phi_0} \gamma_{i,\ell}^{\text{tar}} \mathbf{a}_r(\theta_i^{\text{tar}}) \mathbf{a}_t^{\text{T}}(\theta_i^{\text{tar}}) \mathbf{s}_{\ell,0}(t - 2\tau_i^{\text{tar}}), \quad (3)$$

$$\mathbf{r}_{\ell,k}^{\text{UL}}(t) = \gamma_{k,0}^{\text{u}} \mathbf{a}_r(\theta_{r,k}^{\text{u}}) (\mathbf{a}_{k,t}^{\text{u}}(\theta_{k,t}^{\text{u}}))^{\text{T}} \mathbf{s}_{k,\ell}(t - \tau_k^{\text{u}}) + \sum_{j \in \Phi_k} \gamma_{k,j,\ell}^{\text{tar}} \mathbf{a}_r(\theta_j^{\text{tar}}) (\mathbf{a}_{k,t}^{\text{u}}(\theta_{k,j}^{\text{u}}))^{\text{T}} \mathbf{s}_{k,\ell}(t - \phi_{k,j}). \quad (4)$$

In (3) and (4), Φ_0 is the set of target indices monitored by the DFRC BS, while Φ_k represents the target indices observed by the k^{th} user, expressed as $\Phi_k = [u_1^{(k)}, \dots, u_{|\Phi_k|}^{(k)}]$ for each $k \in \mathcal{K}$. The union of target indices observed by the DFRC BS and all users covers the set of P targets. Generally, the number of targets observed by each user satisfies, with $|\Phi_k| \leq |\Phi_0|$ for $k \in \mathcal{K}$, and the set of targets for different users are distinct, i.e., $\Phi_i \neq \Phi_j$ for $i \neq j$. In addition, $\gamma_{i,\ell}^{\text{tar}} = g_{i,\ell}^{\text{tar}} e^{-j2\pi f_c 2\tau_i^{\text{tar}}} e^{j2\pi f_{D,i} \ell T}$, $g_{i,\ell}^{\text{tar}}$ is the gain of the echo channel between the i^{th} target and the DFRC BS, τ_i^{tar} is the one-way delay between the DFRC BS and the i^{th} target, $f_{D,i}$ is the doppler frequency due to the i^{th} target, $\gamma_{k,0}^{\text{u}} = g_{k,0}^{\text{u}} e^{-j2\pi f_c \tau_k^{\text{u}}}$, $g_{k,0}^{\text{u}}$ is the channel gain between the k^{th} user and the DFRC BS, τ_k^{u} is the delay between the DFRC BS and the k^{th} user, θ_k^{u} is the AoD of the direct path from the user, $\theta_{r,k}^{\text{u}}$ is the AoA of the direct path at the DFRC BS, $\gamma_{k,j,\ell}^{\text{tar}} = g_{k,j,\ell}^{\text{tar}} e^{-j2\pi f_c \phi_{k,j}} e^{j2\pi f_{D,j} \ell T}$, $g_{k,j,\ell}^{\text{tar}}$ is the channel gain between the k^{th} user, j^{th} target and the DFRC BS, $\phi_{k,j}$ is the delay between the k^{th} user, j^{th} target and the DFRC BS, and $\theta_{k,j}^{\text{tar}}$ is the AoD of the UL signal from the k^{th} user towards the j^{th} target. In addition, $\mathbf{a}_r(\theta)$ is the receiving steering vector at the DFRC BS, $\mathbf{a}_t(\theta) \in \mathbb{C}^{N \times 1}$ is the transmit steering vector at the DFRC BS, and $\mathbf{a}_{k,t}^{\text{u}}(\theta) \in \mathbb{C}^{N_k^{\text{u}} \times 1}$ is the transmit steering vector of the k^{th} user. A general expression of the steering response of the n^{th} antenna due to a signal arriving or departing at an angle θ is given in [24]. In this work, following a *narrowband assumption*, the steering response is given as $a_n(\theta) = \exp(j2\pi \frac{d}{\lambda} (n-1) \sin(\theta))$. The received signal is then passed through an ADC, consisting of three parts: pre-filter, sampling, and quantizer [25]. After pre-filtering, the

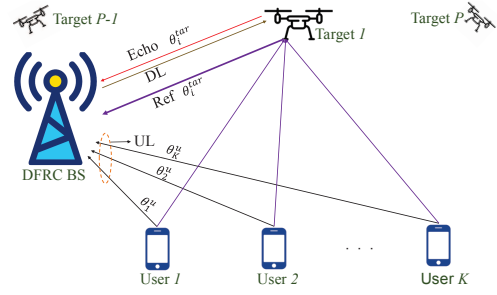


Fig. 1: HRF system model consisting of a DFRC BS operating in monostatic mode, receiving echo from P radar targets, and UL signals from K users.

signal is sampled at regular intervals of $v \triangleq v \frac{T}{M}$ before passing through a quantizer. The sampled signal is, therefore, given as $\mathbf{r}_{\ell}[v] = \mathbf{x}_{\ell}[v] + \mathbf{z}_{\ell}[v]$, where

$$\mathbf{x}_{\ell}[v] = \sum_{\substack{i \in \Phi_0, \\ m_1 \in \mathcal{C}_0}} b_{m_1,0}^{\ell} \mathbf{H}_{\ell,m_1,i}^{\text{echo}} [v] \mathbf{f} + \sum_{\substack{k=1, \\ m_2 \in \mathcal{C}_k}}^K b_{m_2,k}^{\ell} \mathbf{H}_{\ell,m_2,k}^{\text{dp}} [v] \mathbf{f}_k^{\text{u}} + \sum_{\substack{k=1, \\ m_2 \in \mathcal{C}_k}}^K \sum_{j \in \Phi_k} b_{m_2,k}^{\ell} \mathbf{H}_{\ell,m_2,k,j}^{\text{ref}} [v] \mathbf{f}_k^{\text{u}}. \quad (5)$$

$\mathbf{r}_{\ell}[v] \in \mathbb{C}^{N \times 1}$ is a vector of the received signal at the DFRC BS, $\mathbf{H}_{\ell,m_1,i}^{\text{echo}} \in \mathbb{C}^{N \times N}$ is the two-way backscattered channel between the DFRC BS and the i^{th} target for ℓ^{th} symbol on m_1^{th} subcarrier, $\mathbf{H}_{\ell,m_2,k}^{\text{dp}} \in \mathbb{C}^{N \times N_k^{\text{u}}}$ represents the channel of the direct path between the BS and the k^{th} user for ℓ^{th} symbol on m_2^{th} subcarrier, and $\mathbf{H}_{\ell,m_2,k,j}^{\text{ref}} \in \mathbb{C}^{N \times N_k^{\text{u}}}$ denotes the channel of the UL signal transmitted by k^{th} user, reflected by the j^{th} target, and reached at the DFRC BS for ℓ^{th} symbol on m_2^{th} subcarrier. The expressions of all three channels are given as follows.

$$\mathbf{H}_{\ell,m,i}^{\text{echo}} [v] = \tilde{\gamma}_{i,\ell}^{\text{tar}} c_m(2\tau_i^{\text{tar}}, v) \mathbf{a}_r(\theta_i^{\text{tar}}) (\mathbf{a}_t(\theta_i^{\text{tar}}))^{\text{T}}, \quad (6)$$

$$\mathbf{H}_{\ell,m,k}^{\text{dp}} [v] = g_{k,0}^{\text{u}} c_m(\tau_k^{\text{u}}, v) \mathbf{a}_r(\theta_{r,k}^{\text{u}}) (\mathbf{a}_{k,t}^{\text{u}}(\theta_{k,t}^{\text{u}}))^{\text{T}}, \quad (7)$$

$$\mathbf{H}_{\ell,m,k,j}^{\text{ref}} [v] = \tilde{\gamma}_{k,j,\ell}^{\text{tar}} c_m(\phi_{k,j}, v) \mathbf{a}_r(\theta_j^{\text{tar}}) (\mathbf{a}_{k,t}^{\text{u}}(\theta_{k,j}^{\text{u}}))^{\text{T}}, \quad (8)$$

where $\tilde{\gamma}_{i,\ell}^{\text{tar}} = \tilde{\gamma}_{i,\ell}^{\text{tar}} e^{j2\pi f_{D,i} \ell T}$, $c_m(\tau, v) = e^{-j2\pi((m\Delta_f + f_c)\tau - mv/M)}$, $\tilde{\gamma}_{k,j,\ell}^{\text{tar}} = g_{k,j,\ell}^{\text{tar}} e^{j2\pi f_{D,j} \ell T}$. In addition, the UL channel between the k^{th} user and the DFRC BS is characterized as $\mathbf{H}_{\ell,m,k}^{\text{UL}} = \mathbf{H}_{\ell,m,k}^{\text{dp}} + \sum_{j=1}^P \mathbf{H}_{\ell,m,k,j}^{\text{ref}}$.

The time-sampled signal is processed through a b bit scalar quantizer, $\mathcal{Q}(\cdot)$. Given the scalar nature of the quantizer, the real and imaginary components are quantized separately. Consequently, the quantized output at time v can be written as $\mathbf{r}_{\ell}^{\text{q}}[v] = \mathcal{Q}(\mathbf{r}_{\ell}[v])$. Hereafter, the superscript ‘q’ indicates a quantized signal. Additionally, we assume the quantizer inputs are Gaussian, and optimal quantization is applied based on the input distribution [26].

III. QUANTIZED CRB DERIVATION FOR HRF

This section focuses on deriving the quantized CRB for estimating the sensing parameters in the HRF system using the quantized signal $\mathbf{r}_{\ell}^{\text{q}}$. Let $\boldsymbol{\psi} = [\theta_i^{\text{tar}}, f_{D,i}, \tau_i^{\text{tar}}, \theta_{r,k}^{\text{u}}, \theta_k^{\text{u}}, \tau_k^{\text{u}}, \phi_{k,j}, \theta_{k,j}^{\text{u}}, g_{i,\ell}^{\text{tar}}, g_{k,0}^{\text{u}}, g_{k,j}^{\text{u}}] \forall k \in \mathcal{K}, i, j \in \Phi_0$ denote the vector of unknown deterministic parameters to be estimated, and $p(\mathbf{r}_{\ell}^{\text{q}} | \mathbf{x}_{\ell}(\boldsymbol{\psi}))$ represent the likelihood function associated with the quantized signal, which is $p(\mathbf{r}_{\ell}^{\text{q}} | \mathbf{x}_{\ell}(\boldsymbol{\psi})) = \prod_{n=1}^N p(r_{n,\ell}^{\text{q}} | x_{n,\ell}(\boldsymbol{\psi})) = \prod_{n=1}^N p(u_{n,\ell} | x_{n,\ell}(\boldsymbol{\psi})) \prod_{n=1}^N p(w_{n,\ell} | x_{n,\ell}(\boldsymbol{\psi}))$, where $r_{n,\ell}^{\text{q}}$,

$u_{n,\ell}$ and $w_{n,\ell}$ are the n^{th} elements of \mathbf{r}_ℓ^q , $\mathcal{Q}(\Re[\mathbf{r}_\ell])$ and $\mathcal{Q}(\Im[\mathbf{r}_\ell])$, respectively. We denote $x_{n,\ell}^R$ as $\Re[x_{n,\ell}(\boldsymbol{\psi})]$ and $x_{n,\ell}^I$ as $\Im[x_{n,\ell}(\boldsymbol{\psi})]$, where $x_{n,\ell}$ is the n^{th} element of \mathbf{x}_ℓ . The FIM of the real part is similar to that of the imaginary part. Therefore, we consider finding the expression of the FIM considering the real part. To this end, $p(u_{n,\ell} = \delta_b | x_{n,\ell}^R)$ denoted as $p_{u_{n,\ell}}^b$, where δ_b is the quantizer output of the b bit quantizer is written as

$$p_{u_{n,\ell}}^b = \Phi(\alpha_{n,\ell,b}^R) - \Phi(\beta_{n,\ell,b}^R), \quad (9)$$

Where $\alpha_{n,\ell,b}^R = (\omega_b - x_{n,\ell}^R) / (\sigma/\sqrt{2})$, $\beta_{n,\ell,b}^R = (\kappa_b - x_{n,\ell}^R) / (\sigma/\sqrt{2})$, κ_b and ω_b are the lower and upper bounds of the quantization region that contains δ_b , $\Phi(x) = \int_{-\infty}^x \varphi(t)dt$, and $\varphi(x) = (1/\sqrt{2\pi}) e^{-x^2/2}$ which is the PDF of a standard real normal random variable. Similar expression can be obtained for $p(w_{n,\ell} = \delta_b | x_{n,\ell}^I)$ denoted as $p_{w_{n,\ell}}^b$ in which $\alpha_{n,\ell,b}^I = (\omega_b - x_{n,\ell}^I) / (\sigma/\sqrt{2})$, $\beta_{n,\ell,b}^I = (\kappa_b - x_{n,\ell}^I) / (\sigma/\sqrt{2})$. The log-likelihood of $p(\mathbf{r}^q | \mathbf{x}(\boldsymbol{\psi}))$, where $\mathbf{r}^q \in \mathbb{C}^{NL \times 1}$ and $\mathbf{x}(\boldsymbol{\psi}) \in \mathbb{C}^{NL \times 1}$ is

$$\ln(p(\mathbf{r}^q | \mathbf{x}(\boldsymbol{\psi}))) = \sum_{n=1, \ell=1}^{N,L} \ln(p_{u_{n,\ell}}^b) + \ln(p_{w_{n,\ell}}^b). \quad (10)$$

We evaluate the FIM for the real part of the signal for simplicity. A similar expression can be obtained for the imaginary part as well. Furthermore, we use the additivity of the contributions of the real and imaginary parts of the FIMs to obtain the final FIM. To this end, the $(i, j)^{\text{th}}$ entry of the FIM of the real part for a b -bit quantizer is $[\mathbf{F}_{u_{n,\ell}}(\boldsymbol{\psi})]_{ij} = \mathbb{E} \left\{ \frac{\partial \ln p_{u_{n,\ell}}^b}{\partial \psi_i} \frac{\partial \ln p_{u_{n,\ell}}^b}{\partial \psi_j} \right\}$. Furthermore, using (9),

$$\frac{\partial \ln p_{u_{n,\ell}}^b}{\partial \psi_i} = -\frac{\sqrt{2}}{\sigma} \frac{[\varphi(\alpha_{n,\ell,b}^R) - \varphi(\beta_{n,\ell,b}^R)]}{p_{u_{n,\ell}}^b} \frac{\partial x_{n,\ell}^R}{\partial \psi_i}. \quad (11)$$

From (11) and (9),

$$[\mathbf{F}_{u_{n,\ell}}]_{ij} = \mathbb{E} \left[\frac{2}{\sigma^2} \frac{\partial x_{n,\ell}^R}{\partial \psi_i} \frac{\partial x_{n,\ell}^R}{\partial \psi_j} \frac{[\varphi(\alpha_{n,\ell,b}^R) - \varphi(\beta_{n,\ell,b}^R)]^2}{(p_{u_{n,\ell}}^b)^2} \right] \quad (12)$$

$$[\mathbf{F}_{u_{n,\ell}}]_{ij} = \frac{2}{\sigma^2} \frac{\partial x_{n,\ell}^R}{\partial \psi_i} \frac{\partial x_{n,\ell}^R}{\partial \psi_j} \Lambda_{n,\ell,b}^R,$$

where $\Lambda_{n,\ell,b}^y = \frac{[\varphi(\alpha_{n,\ell,b}^y) - \varphi(\beta_{n,\ell,b}^y)]^2}{\Phi(\alpha_{n,\ell,b}^y) - \Phi(\beta_{n,\ell,b}^y)}$, $y \in \{R, I\}$. We have to note that (12) has been derived considering one OFDM symbol, one antenna element, and one quantization region. Therefore, when we consider the total number of received symbols, L , N antennas, and $B = 2^b$ quantization regions, the FIM is given as follows

$$[\mathbf{F}_{\mathbf{u}}]_{ij} = \sum_{\ell=1}^L \sum_{n=1}^N \sum_{b=1}^B \frac{2}{\sigma^2} \frac{\partial x_{n,\ell}^R}{\partial \psi_i} \frac{\partial x_{n,\ell}^R}{\partial \psi_j} \Lambda_{n,\ell,b}^R, \quad (13)$$

where $\mathbf{u} \in \mathbb{R}^{NL \times 1}$. However, (13) is derived for the real part of the quantized signal, and a similar expression can be obtained for the imaginary part, which is given as

$$[\mathbf{F}_{\mathbf{w}}]_{ij} = \sum_{\ell=1}^L \sum_{n=1}^N \sum_{b=1}^B \frac{2}{\sigma^2} \frac{\partial x_{n,\ell}^I}{\partial \psi_i} \frac{\partial x_{n,\ell}^I}{\partial \psi_j} \Lambda_{n,\ell,b}^I, \quad (14)$$

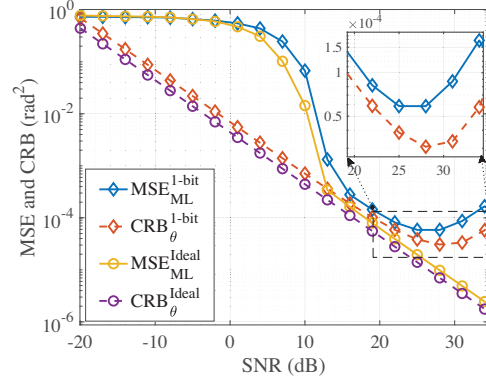


Fig. 2: MSE of ML estimator and CRB versus SNR for ideal and 1-bit ADC.

where $\mathbf{w} \in \mathbb{R}^{NL \times 1}$. We use the additivity property of the real and imaginary FIMs to write the final expression of the FIM of $\mathbf{r}^q(\boldsymbol{\psi}) \in \mathbb{C}^{NL \times 1}$ which is written as

$$[\mathbf{F}_{\mathbf{r}^q}]_{ij} = [\mathbf{F}_{\mathbf{u}}]_{ij} + [\mathbf{F}_{\mathbf{w}}]_{ij}. \quad (15)$$

CRB is the inverse of the FIM. Therefore, CRB of a parameter ψ_i , $\text{CRB}_{\psi_i} = \left([\mathbf{F}_{\mathbf{r}^q}(\boldsymbol{\psi})]^{-1} \right)_{ii}$. The FIM using ideal or infinite resolution ADC is given as

$$[\mathbf{F}_{\mathbf{r}}]_{ij}^\infty = \frac{2}{\sigma^2} \sum_{\ell=1}^L \sum_{n=1}^N \left(\frac{\partial x_{n,\ell}^R}{\partial \psi_i} \frac{\partial x_{n,\ell}^R}{\partial \psi_j} + \frac{\partial x_{n,\ell}^I}{\partial \psi_i} \frac{\partial x_{n,\ell}^I}{\partial \psi_j} \right). \quad (16)$$

In the context of HRF, the partial derivatives of the real and imaginary components of $x_{n,\ell}(\boldsymbol{\psi})$ with ψ_i , i.e., $\partial x_{n,\ell}^R / \partial \psi_i$ and $\partial x_{n,\ell}^I / \partial \psi_i$, can be computed using the expressions for $\partial x_{n,\ell} / \partial \psi_i$ provided in Appendix A for all sensing parameters of the HRF system.

The next step is to verify the correctness of the derived CRB expression and its corresponding derivatives. We do this by plotting the CRB alongside the MSE of the Maximum Likelihood (ML) estimator on the same plot. The verification process leverages the fact that the MSE of any unbiased estimator converges to the CRB at a high signal-to-noise ratio (SNR). Using the derivatives from Appendix A and the CRB expression in Equation (15), we validate the CRB for the AoA. For this verification, we consider a simple scenario involving a single target ($P = 1$) and a single user ($K = 1$) interacting with a DFRC BS. The target is assumed to approach the DFRC BS from an angle $\theta = 30^\circ$. The BS transmits a DL probing signal and receives the corresponding echo while simultaneously receiving a UL signal from the user, as shown in 1. In this setting, we maximize the likelihood function in (10) for a 1-bit ADC via grid search. Additionally, we consider a likelihood function that disregards the effects of quantization for comparison [24]. We plot the MSE and CRB for both the quantized and unquantized cases, as shown in Fig. 2. At high SNR, the MSE of the ML estimator converges to the CRB in both cases, affirming the correctness of our CRB derivation. Furthermore, we observe a peculiar behavior: after a certain SNR threshold, the MSE of the ML estimator and CRB for the 1-bit quantization case begin to increase and diverge. This phenomenon, known as stochastic resonance [27], is discussed in detail in the following subsection.

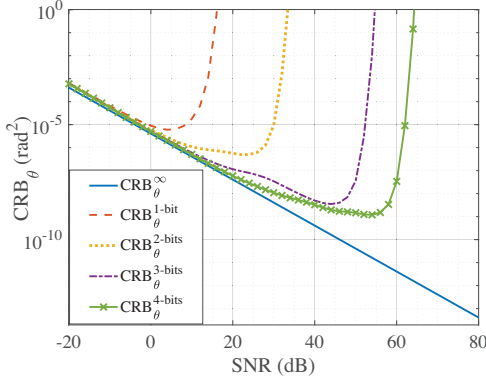


Fig. 3: stochastic resonance demonstrated through CRB_θ for a HRF system.

A. HRF stochastic Resonance

Fig. 3 illustrates the phenomenon of stochastic resonance, where noise, under specific conditions, enhances rather than degrades the system performance. This counter-intuitive effect challenges the traditional view of noise as detrimental to signal processing and estimation accuracy. In Fig. 3, we plot CRB_θ for $P = 1$, $K = 1$, $\theta = 0^\circ$, and ADC resolutions $b = \{1, 2, 3, 4\}$, showing the non-monotonic behavior of CRB with varying SNR. Notably, each ADC resolution has an optimal SNR at which CRB is minimized, achieving peak estimation accuracy. This finding supports existing literature on stochastic resonance [27] and underscores the role of ADC resolution in ISAC systems. The presence of an optimal SNR for each ADC resolution emphasizes the need to jointly optimize signal and ADC parameters for minimum estimation error in HRF systems. *Moreover, this optimal SNR may shift with changes in the CRB expression or system parameters, potentially defining distinct SNRs for tasks like channel estimation in communication. This insight is critical for ISAC system design, balancing sensing and communication within hardware constraints such as ADC resolution.*

B. Lower bound on FIM of HRF

To investigate the impact of ADC DR on HRF systems via CRB-rate boundaries, we formulate optimization problems that allow us to quantify these boundaries. However, the complexity of the FIM expression in (15) hinders us from directly using it for optimization. Given the dual objective of optimizing the sensing CRB and communication rates, lower bounds on the FIM and rate offer more tractable alternatives. Therefore, we derive a lower bound on FIM using a method analogous to that proposed in [28]. To this end, we leverage the Bussgang theorem [29], which allows the quantized signal to be modeled as a linear system. The Bussgang theorem is particularly applicable to Gaussian signals propagating through nonlinear systems. Given that quantization is inherently nonlinear, the Bussgang theorem facilitates the decomposition of the received signal into two components: a linear function of the input and a quantization noise term uncorrelated with the input. Accordingly, the quantized signal can be expressed as $\mathbf{r}_\ell^q = \mathbf{G}\mathbf{r}_\ell + \mathbf{z}_\ell^q$, where \mathbf{G} is the distortion matrix and \mathbf{z}_ℓ^q represents the uncorrelated quantization noise vector. The distortion matrix \mathbf{G} is derived under the assumption that \mathbf{r}_ℓ and \mathbf{z}_ℓ^q are uncorrelated, making \mathbf{G} the LMMSE estimate

of \mathbf{r}_ℓ^q from \mathbf{r}_ℓ . Consequently, $\mathbf{G} = \mathbb{E}[\mathbf{r}_\ell^q \mathbf{r}_\ell^H] \mathbb{E}[\mathbf{r}_\ell \mathbf{r}_\ell^H]^{-1} = \mathbf{R}_{\mathbf{r}_\ell^q \mathbf{r}_\ell} \mathbf{R}_{\mathbf{r}_\ell \mathbf{r}_\ell}^{-1}$, where $\mathbf{R}_{\mathbf{r}_\ell \mathbf{r}_\ell} = \mathbf{R}_{\mathbf{x}_\ell \mathbf{x}_\ell} + \mathbf{R}_{\mathbf{z}_\ell \mathbf{z}_\ell}$. The computation of covariance matrix $\mathbf{R}_{\mathbf{x}_\ell \mathbf{x}_\ell} \triangleq \mathbb{E}[\mathbf{x}_\ell \mathbf{x}_\ell^H]$ is provided in Appendix B and the expression is given in (45). Furthermore, the covariance matrix of the quantization noise, \mathbf{z}_ℓ^q is $\mathbf{R}_{\mathbf{z}_\ell^q \mathbf{z}_\ell^q} = \mathbb{E}[(\mathbf{r}_\ell^q - \mathbf{G}\mathbf{r}_\ell)(\mathbf{r}_\ell^q - \mathbf{G}\mathbf{r}_\ell)^H] = \mathbf{R}_{\mathbf{r}_\ell^q \mathbf{r}_\ell^q} - \mathbf{R}_{\mathbf{r}_\ell^q \mathbf{r}_\ell} \mathbf{R}_{\mathbf{r}_\ell \mathbf{r}_\ell}^{-1} \mathbf{R}_{\mathbf{r}_\ell \mathbf{r}_\ell^q}$. Additionally, the quantized signal, \mathbf{r}_ℓ^q can be expressed as $\mathbf{r}_\ell^q = \mathbf{G}\mathbf{x}_\ell + \mathbf{G}\mathbf{z}_\ell + \mathbf{z}_\ell^q = \mathbf{G}\mathbf{x}_\ell + \bar{\mathbf{z}}_\ell$, where $\bar{\mathbf{z}}_\ell$ is the effective noise after quantization. Although the effective noise distribution is not necessarily Gaussian, its covariance matrix can be computed as $\mathbf{R}_{\bar{\mathbf{z}}_\ell \bar{\mathbf{z}}_\ell} = \mathbf{G}\mathbf{R}_{\mathbf{z}_\ell \mathbf{z}_\ell} \mathbf{G}^H + \mathbf{R}_{\mathbf{z}_\ell^q \mathbf{z}_\ell^q}$. Let η denote the distortion factor introduced by each quantizer at the receiver. It is established that for Gaussian channel inputs, all signal samples experience uniform distortion [30]. Consequently, $\mathbf{G} = (1 - \eta) \mathbf{I}_N$. The distortion factor η for both uniform and non-uniform quantizers is calculated in [31] for various ADC resolutions, specifically in the context of Gaussian-distributed signals. Moreover, approximate covariance matrices for the effective noise and quantized signal are provided in [30]. Therefore, under the assumption of Gaussian-distributed channel inputs, the approximate covariance matrices for the effective noise and quantized signal are given as

$$\mathbf{R}_{\bar{\mathbf{z}}_\ell \bar{\mathbf{z}}_\ell}^{\text{approx}} \approx (1 - \eta)^2 \mathbf{R}_{\mathbf{z}_\ell \mathbf{z}_\ell} + \eta(1 - \eta) \text{diag}(\mathbf{R}_{\mathbf{r}_\ell \mathbf{r}_\ell}), \quad (17)$$

$$\mathbf{R}_{\mathbf{r}_\ell^q \mathbf{r}_\ell^q}^{\text{approx}} \approx (1 - \eta)^2 \mathbf{R}_{\mathbf{r}_\ell \mathbf{r}_\ell} + \eta(1 - \eta) \text{diag}(\mathbf{R}_{\mathbf{r}_\ell \mathbf{r}_\ell}). \quad (18)$$

To derive the lower bound on the FIM, the condition $\partial \mathbf{R}_{\bar{\mathbf{z}}_\ell \bar{\mathbf{z}}_\ell} / \partial \psi = 0$ must be satisfied. Furthermore, at low per-antenna SNR, this condition is satisfied, where $\mathbf{R}_{\mathbf{r}_\ell \mathbf{r}_\ell} \approx \mathbf{R}_{\mathbf{z}_\ell \mathbf{z}_\ell}$. The low per-antenna SNR assumption is valid as this is true in practice for mmWave systems [32]. Consequently, the covariance matrices for the effective noise and the quantized signal are given by

$$\mathbf{R}_{\bar{\mathbf{z}}_\ell \bar{\mathbf{z}}_\ell}^{\text{LS}} \approx (1 - \eta)^2 \mathbf{R}_{\mathbf{z}_\ell \mathbf{z}_\ell} + \eta(1 - \eta) \text{diag}(\mathbf{R}_{\mathbf{z}_\ell \mathbf{z}_\ell}), \quad (19)$$

$$\mathbf{R}_{\mathbf{r}_\ell^q \mathbf{r}_\ell^q}^{\text{LS}} \approx (1 - \eta)^2 \mathbf{R}_{\mathbf{z}_\ell \mathbf{z}_\ell} + \eta(1 - \eta) \text{diag}(\mathbf{R}_{\mathbf{z}_\ell \mathbf{z}_\ell}), \quad (20)$$

where LS denotes the low SNR assumption. According to the results presented in [28] and [32], the lower bound of the FIM can be written as

$$[\mathbf{F}_{\mathbf{r}_\ell^q}^{\text{LS}}]_{ij} \geq 2\Re \left[\sum_{\ell=1}^L \left(\frac{\partial \mathbf{G}\mathbf{x}_\ell}{\partial \psi_i} \right)^H \left(\mathbf{R}_{\bar{\mathbf{z}}_\ell \bar{\mathbf{z}}_\ell}^{\text{LS}} \right)^{-1} \left(\frac{\partial \mathbf{G}\mathbf{x}_\ell}{\partial \psi_j} \right) \right]. \quad (21)$$

In the case, where $\mathbf{R}_{\mathbf{z}_\ell \mathbf{z}_\ell} = \sigma^2 \mathbf{I}_N$, the covariance matrix simplifies to $\mathbf{R}_{\bar{\mathbf{z}}_\ell \bar{\mathbf{z}}_\ell}^{\text{LS}} = \sigma^2 (1 - \eta) \mathbf{I}_N$. Therefore, in this scenario, (21) simplifies to

$$[\mathbf{F}_{\mathbf{r}_\ell^q}^{\text{LS}}]_{ij} \geq \frac{2(1 - \eta)}{\sigma^2} \Re \left[\sum_{\ell=1}^L \sum_{n=1}^N \left(\frac{\partial x_{n,\ell}(\boldsymbol{\psi})}{\partial \psi_i} \right)^* \left(\frac{\partial x_{n,\ell}(\boldsymbol{\psi})}{\partial \psi_j} \right) \right]. \quad (22)$$

IV. LOWER BOUND ON RATE AND 1-BIT QUANTIZATION

In this section, we derive the lower bound on the UL rate. As mentioned in [33], for a given covariance matrix, the mutual information (MI) is minimized when the effective noise vector $\bar{\mathbf{z}}_\ell$ is Gaussian distributed. Leveraging this result, we calculate the lower bound on the UL rate for the HRF system. The approximate covariance matrices for the effective noise and the quantized signal are specified in (17) and (18), respectively. Using these expressions, the lower bound on the rate of the HRF system is given by

$$I(s_\ell; \mathbf{r}_\ell^q) \geq \log_2 \left| \mathbf{I}_N + \left(\mathbf{R}_{\bar{\mathbf{z}}_\ell \bar{\mathbf{z}}_\ell}^{\text{approx}} \right)^{-1} (1 - \eta)^2 \mathbf{R}_{\mathbf{x}_\ell \mathbf{x}_\ell} \right|. \quad (23)$$

For the low SNR scenario, $\mathbf{R}_{\bar{\mathbf{z}}_\ell \bar{\mathbf{z}}_\ell}^{\text{approx}}$ is substituted with $\mathbf{R}_{\bar{\mathbf{z}}_\ell \bar{\mathbf{z}}_\ell}^{\text{LS}}$. Additionally, when $\mathbf{R}_{\mathbf{z}_\ell \mathbf{z}_\ell} = \sigma^2 \mathbf{I}_N$ and $\mathbf{R}_{\bar{\mathbf{z}}_\ell \bar{\mathbf{z}}_\ell}^{\text{LS}} = \sigma^2 (1 - \eta) \mathbf{I}_N$, the rate equation simplifies to

$$I(\mathbf{s}_\ell; \mathbf{r}_\ell^q) \geq \log_2 \left| \mathbf{I}_N + \left(\frac{1 - \eta}{\sigma^2} \right) \mathbf{R}_{\mathbf{x}_\ell \mathbf{x}_\ell} \right|. \quad (24)$$

A. 1-bit Quantization

In this subsection, we consider the case of symmetric 1-bit ADC as we can derive exact expressions for the covariance matrices of both the effective noise and the quantized signal. These derivations are based on the arcsine law as detailed in [34]. Using the results obtained in [34] and [30], the covariance matrix for the quantized signal and the covariance matrix between the input and output of the 1-bit quantizer for the HRF system can be written as

$$\mathbf{R}_{\mathbf{r}_\ell^q \mathbf{r}_\ell^q} = \frac{2}{\pi} \sin^{-1} \left[\text{diag}(\mathbf{R}_{\mathbf{r}_\ell \mathbf{r}_\ell})^{-\frac{1}{2}} \mathbf{R}_{\mathbf{r}_\ell \mathbf{r}_\ell} \text{diag}(\mathbf{R}_{\mathbf{r}_\ell \mathbf{r}_\ell})^{-\frac{1}{2}} \right], \quad (25)$$

$$\mathbf{R}_{\mathbf{r}_\ell^q \mathbf{r}_\ell} = \sqrt{2/\pi} \text{diag}(\mathbf{R}_{\mathbf{r}_\ell \mathbf{r}_\ell})^{-1/2} \mathbf{R}_{\mathbf{r}_\ell \mathbf{r}_\ell}. \quad (26)$$

From the expressions in (25) and (26), the distortion matrix \mathbf{G} can be represented as $\mathbf{G} = \sqrt{2/\pi} \text{diag}(\mathbf{R}_{\mathbf{r}_\ell \mathbf{r}_\ell})^{-1/2}$ and the covariance of the effective noise can be written as

$$\begin{aligned} \mathbf{R}_{\bar{\mathbf{z}}_\ell \bar{\mathbf{z}}_\ell} &= \frac{2}{\pi} \arcsin \left(\text{diag}(\mathbf{R}_{\mathbf{r}_\ell \mathbf{r}_\ell})^{-1/2} \mathbf{R}_{\mathbf{r}_\ell \mathbf{r}_\ell} \text{diag}(\mathbf{R}_{\mathbf{r}_\ell \mathbf{r}_\ell})^{-1/2} \right) \\ &\quad - \frac{2}{\pi} \text{diag}(\mathbf{R}_{\mathbf{r}_\ell \mathbf{r}_\ell})^{-1/2} \mathbf{R}_{\mathbf{r}_\ell \mathbf{r}_\ell} \text{diag}(\mathbf{R}_{\mathbf{r}_\ell \mathbf{r}_\ell})^{-1/2} \\ &\quad + \frac{2}{\pi} \text{diag}(\mathbf{R}_{\mathbf{r}_\ell \mathbf{r}_\ell})^{-1/2} \mathbf{R}_{\mathbf{z}_\ell \mathbf{z}_\ell} \text{diag}(\mathbf{R}_{\mathbf{r}_\ell \mathbf{r}_\ell})^{-1/2}. \end{aligned} \quad (27)$$

The lower bound on the MI can be computed using the expression in (23). Considering the low per-antenna SNR assumption, the lower bound on the MI can be written as

$$I(\mathbf{s}_\ell; \mathbf{r}_\ell^q)^{1-\text{bit}} \geq \text{tr} \left(\mathbf{R}_{\mathbf{x}_\ell \mathbf{x}_\ell} \text{diag}(\mathbf{R}_{\mathbf{z}_\ell \mathbf{z}_\ell})^{-\frac{1}{2}} \left[\arcsin \left(\text{diag}(\mathbf{R}_{\mathbf{z}_\ell \mathbf{z}_\ell})^{-\frac{1}{2}} \mathbf{R}_{\mathbf{z}_\ell \mathbf{z}_\ell} \text{diag}(\mathbf{R}_{\mathbf{z}_\ell \mathbf{z}_\ell})^{-\frac{1}{2}} \right) \right]^{-1} \text{diag}(\mathbf{R}_{\mathbf{z}_\ell \mathbf{z}_\ell})^{-\frac{1}{2}} \right). \quad (28)$$

When $\mathbf{R}_{\mathbf{z}_\ell \mathbf{z}_\ell} = \sigma^2 \mathbf{I}_N$, (28) simplifies to

$$I(\mathbf{s}_\ell; \mathbf{r}_\ell^q)^{1-\text{bit}} \approx \frac{2}{\pi \sigma^2} \text{tr}(\mathbf{R}_{\mathbf{x}_\ell \mathbf{x}_\ell}). \quad (29)$$

V. OPTIMIZATION FRAMEWORK FOR CRB-UL RATE TRADE-OFF CHARACTERIZATION

In this section, we devise two key optimization problems, denoted as \mathbb{P}_0 and \mathbb{P}_1 , to systematically characterize the CRB-rate boundary for HRF systems. The CRB-rate boundary provides critical insights into the trade-offs between CRB and rate in ISAC systems. To precisely plot this boundary, we employ optimization techniques that leverage the lower bounds on the FIM and rate given in (22) and (24) for CRB and rate computation, respectively. The optimization approach is necessary because the endpoints of the CRB-rate boundary correspond to minimizing the CRB and maximizing the rate, respectively. However, the complete boundary characterization requires balancing these objectives, which can only be achieved by subjecting one of the parameters to constraints while optimizing the other. Hence, we formulate two optimization problems: \mathbb{P}_0 focuses on minimizing the CRB of the sensing parameter while maintaining a threshold on the communication rate to ensure the minimum quality of service (QoS) for the user, and \mathbb{P}_1 maximizes the rate while ensuring an acceptable level of sensing performance.

A. Sensing-Centric design

We hereby formulate the optimization problem \mathbb{P}_0 as follows

$$(\mathbb{P}_0) \quad \underset{\mathbf{f}_0, \{\mathbf{f}_k^u\}_{k=1}^K}{\text{minimize}} \quad (\text{CRB}_{\psi_i}^{\text{LS}}(\mathbf{f}, \mathbf{f}_k^u)) \quad (30a)$$

$$\text{s. t.} \quad \text{tr}(\mathbf{R}_k) \leq P_{\max}^u, \quad \forall k \in \mathcal{K} \quad (30b)$$

$$\text{tr}(\mathbf{R}_0) \leq P_{\max}^{\text{BS}} \quad (30c)$$

$$\text{rank}(\mathbf{R}_0) = 1 \quad (30d)$$

$$\text{rank}(\mathbf{R}_k) = 1, \quad \forall k \in \mathcal{K} \quad (30e)$$

$$I(\mathbf{s}_\ell; \mathbf{r}_\ell^q) \geq \mu \quad (30f)$$

where ψ_i is the parameter of interest, $\text{CRB}_{\psi_i}^{\text{LS}} = \left[(\mathbf{F}_{\mathbf{r}^q}^{\text{LS}})^{-1} \right]_{ii}$, $\mathbf{R}_0 = \mathbf{f}\mathbf{f}^H$ and $\mathbf{R}_k = \mathbf{f}_k^u (\mathbf{f}_k^u)^H$, \mathbf{R}_0 and \mathbf{R}_k are positive semidefinite matrices. The objective function in \mathbb{P}_0 , (30a) minimizes the CRB of the HRF system. Constraints (30b) and (30c) restrict the maximum transmit power of the users and BS to P_{\max}^u and P_{\max}^{BS} , respectively, and are quadratic constraints. In addition, the constraints in (30d) and (30e) are the rank-1 constraints of the precoders of the BS and users, and the MI constraint (30f) ensures a minimum communication rate. Constraints (30d) and (30e) are non-convex. To address this, we use rank-1 relaxation and reformulate \mathbb{P}_0 as follows

$$(\mathbb{P}_0) \quad \underset{\mathbf{R}_0, \{\mathbf{R}_k\}_{k=1}^K}{\text{minimize}} \quad (\text{CRB}_{\psi_i}^{\text{LS}}(\mathbf{R}_0, \mathbf{R}_k)) \quad (31a)$$

$$\text{s. t.} \quad (30b), (30c), (30f),$$

$$\mathbf{R}_0 \succeq 0 \quad (31b)$$

$$\mathbf{R}_k \succeq 0, \quad \forall k \in \mathcal{K}, \quad (31c)$$

This convex problem can now be solved using CVX, allowing us to find the minimum CRB under the given power and rate constraints.

B. Communication-Centric design

We formulate another optimization problem, \mathbb{P}_1 , where the objective of the problem is to maximize the communication rate of the HRF system with a constraint on the CRB of the system. To this end, \mathbb{P}_1 is formulated as follows

$$(\mathbb{P}_1) \quad \underset{\mathbf{f}_0, \{\mathbf{f}_k^u\}_{k=1}^K}{\text{maximize}} \quad I(\mathbf{s}_\ell; \mathbf{r}_\ell^q) \quad (32a)$$

$$\text{s. t.} \quad (\text{CRB}_{\psi_i}^{\text{LS}}(\mathbf{f}, \mathbf{f}_k^u)) \leq \Gamma \quad (32b)$$

$$(30b), (30c), (30d), (30e),$$

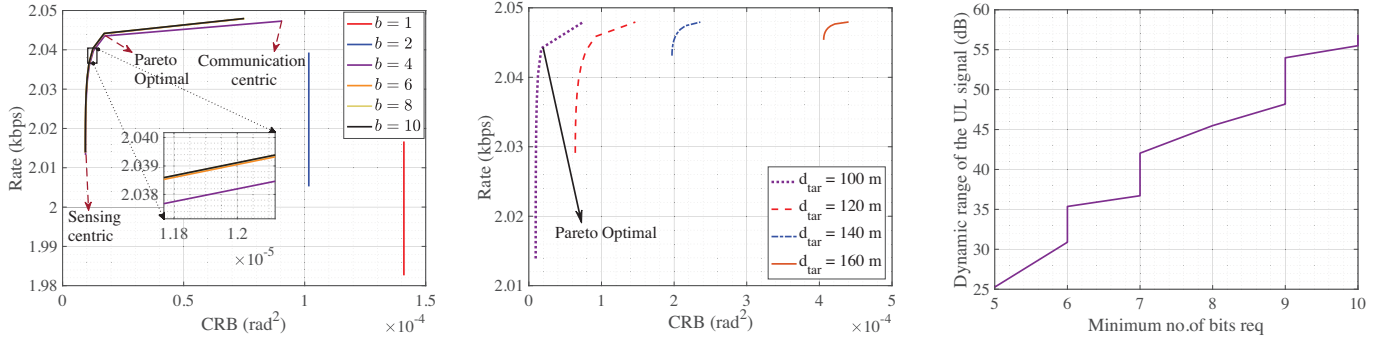
where Γ is the threshold on the CRB. The expression of $I(\mathbf{s}_\ell; \mathbf{r}_\ell^q)$ is given in (24). Constraints (30d) and (30e) are the non-convex constraints, as we have seen in V-A. Therefore, we use rank-1 relaxation and reformulate \mathbb{P}_1 as follows

$$(\mathbb{P}_1) \quad \underset{\mathbf{R}_0, \{\mathbf{R}_k\}_{k=1}^K}{\text{minimize}} \quad I(\mathbf{s}_\ell; \mathbf{r}_\ell^q) \quad (33a)$$

$$\text{s. t.} \quad \text{CRB}_{\psi_i}^{\text{LS}}(\mathbf{R}_0, \mathbf{R}_k) \leq \Gamma \quad (33b)$$

$$(30b), (30c), (31b), (31c),$$

The worst and the best lower bounds on rates are determined by setting $\mu = 0$ in \mathbb{P}_0 and $\Gamma = 0$ in \mathbb{P}_1 , respectively, and solving them using CVX. These two extreme points on the CRB-rate boundary correspond to what we define as the ‘‘sensing-centric’’ and ‘‘communication-centric’’ points. Specifically, when $\mu = 0$ in \mathbb{P}_0 , we obtain a sensing-centric solution that minimizes the upper bound on the CRB while yielding the worst possible rate, as we enforce the lower



(a) CRB vs. UL rate for $K = 1$ and $P = 1$ varying the ADC resolution and fixing the user and target at a distance of 100 m from the DFRC BS.

(b) CRB vs UL rate for $K = 1$ and $P = 1$, fixing the user and varying the distance of the target from the DFRC BS.

(c) DR of the UL signal vs the minimum required ADC resolution to differentiate the reflection and the direct path for $K = 1$ and $P = 1$.

Fig. 4: The trade-off between the CRB and UL rate considering PL.

bound on rate to be just greater than 0. On the other hand, when $\Gamma = 0$ in \mathbb{P}_1 , we achieve the best lower bound on the communication rate but at the cost of the worst CRB. In this case, the CRB is constrained to be just greater than 0, and since we use its upper bound in the formulation, maximizing the rate while setting the upper bound on CRB greater than zero leads to this communication-centric solution. This point reflects the scenario where the system prioritizes communication throughput over sensing accuracy. The CRB-rate boundary is then generated by sweeping the value of μ in \mathbb{P}_1 between the worst and the best lower bounds on rate, providing a comprehensive characterization of the trade-off between sensing accuracy and communication throughput. This approach allows us to quantify the performance limits of the HRF system for different ADC resolutions and power constraints.

VI. RESULTS AND DISCUSSION

In this section, we present our findings derived from extensive simulations. To illustrate the impact of ADC DR and quantization on HRF performance, we focus on the CRB for the AoAs of targets within the observed scene. Specifically, we evaluate the expression of CRB in (22) for the parameters $\psi_i = \theta_i$ and $\psi_j = \theta_j$, with their detailed derivation provided in Appendix C. We first outline the parameter set used to generate the numerical results.

A. Parameter Setup

For clarity, we use a simple simulation setup with a DFRC BS, a single user ($K = 1$), and a single target ($P = 1$). The user is positioned 100 m from the BS at an angle of 10° , while the target is at 50° relative to the BS. For comparative analysis, we vary the target's distance within $\{80, 90, 100, 120, 140, 160\}$ m, while keeping the user fixed at 100 m. These distances are within a typical cell radius for mmWave communications (about 500 m) [35]. The carrier frequency is set to 24 GHz. Both the BS and user employ a uniform linear array (ULA) with $\lambda/2$ antenna spacing; the BS has $N = 8$ antennas for both transmission and reception, while the user has $N_k^u = 4$ transmit antennas. The BS antenna gain is 25 dBi, and the user's transmit gain is 17 dBi. Thermal noise power spectral density is -174 dBm/Hz, with a maximum transmit power of 30 dBm for the BS and 20

dBm for the user. The system uses 14 OFDM symbols, with 72 subcarriers for DL and 60 for UL, each at a 15 kHz bandwidth. Pathloss is computed using equations and parameters in [24]. All simulation parameters align with typical mmWave system values [36] and are used throughout unless otherwise stated.

B. Simulation Results

1) CRB-Rate trade-off considering ADC DR

The simulation in Fig. 4a reveals key insights into the trade-off between CRB and rate in HRF systems, particularly about the impact of ADC DR. The CRB-rate boundaries are plotted for various ADC resolutions by fixing the target at 100 m. For a given ADC, the sensing-centric point on the CRB-rate boundary is obtained by solving the optimization problem \mathbb{P}_0 in (31a) with $\mu = 0$. Conversely, the communication-centric point is determined by solving \mathbb{P}_1 in (32b) with $\Gamma = 0$. The full CRB-rate boundary is then constructed by sweeping the value of μ in (30f) between the worst and best lower bounds on rate, as detailed in V. Here, the Pareto optimal points highlight the best possible trade-off between CRB and rate for each ADC resolution. The ADC DR, as given in [37], is directly related to the resolution of the ADC, b , with a higher resolution corresponding to a greater DR. The CRB-rate boundary is plotted for various b . In particular, the CRB remains unchanged for $b = 1$ and $b = 2$, indicating that the DR of the ADC is insufficient to distinguish the reflected signal from the noise floor. This occurs because the DR of the UL signal, defined as

$$\text{DR}_{\text{sig}} = 10 \log_{10} \left(P_k^{\text{dp}} / P_{k,j}^{\text{ref}} \right), \quad (34)$$

where P_k^{dp} is the power of the direct path of the user k^{th} and $P_{k,j}^{\text{ref}}$ is the power of the reflected signal of the user k^{th} and the target j^{th} , exceeds the DR of the ADC for these resolutions. Consequently, the weaker reflected signal is indistinguishable from the noise floor, inhibiting the possibility of effective HRF at the DFRC BS. However, at $b = 4$ bits, the CRB begins to vary with the rate, reflecting the ADC's enhanced ability to distinguish the reflected signal from the noise with increased resolution. Therefore, the DFRC BS can perform HRF. This is illustrated by the change in the CRB with μ in \mathbb{P}_0 . As μ changes, the power levels of the direct and reflected signals are adjusted, influencing the DR of the signal.

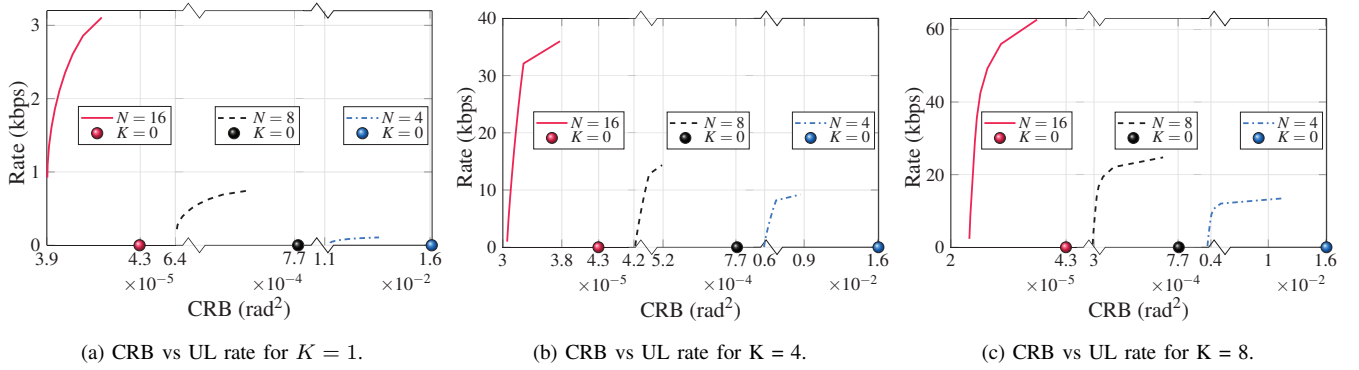


Fig. 5: CRB-rate trade-off for different numbers of users as the BS antenna array size increases.

However, for lower resolutions ($b = 1$ bits and $b = 2$ bits), the CRB remains constant even as μ varies, reinforcing the ADC's inability to distinguish the weaker signal despite the adjusted DR for different μ . In contrast, at higher resolutions ($b \geq 4$ bits), the DR of the ADC increases sufficiently to allow the BS to differentiate the weaker reflected signal from noise and successfully perform HRF. Moreover, as b increases, the CRB decreases, and the rate improves. However, beyond a certain resolution, the improvements in CRB and rate become marginal, "suggesting that more bits become unnecessary."

2) Impact of target distance on the CRB-rate trade-off

In contrast, the CRB decreases when the target is closer to the BS. In this scenario, despite the reduced distance between the user and the target, the transmit power of the BS becomes the dominant factor, thus lowering the CRB and improving the sensing performance. However, when the BS power is overly dominant, the gains from HRF become marginal. Thus, we can conclude that a trade-off exists between the echo power and the reflected signal power received at the BS, significantly impacting the HRF gains. This is also observed and mentioned in [24]. The plot in Fig. 4b shows the CRB-rate boundary as a function of the target distance from the BS for an ADC resolution of $b = 14$ bits. The results indicate that the CRB increases as the target moves farther from the BS while the user's position remains fixed. This trend is due to the increased attenuation of the reflected UL signal as the target distance increases. Additionally, as the target distance grows, so does the user-target distance, further attenuating the reflected UL signal and contracting the CRB-rate boundary.

As the target distance increases from 100 m to 160 m, Pareto optimal points shift towards higher CRB values, emphasizing the trade-off between CRB and rate with distance. At 100 m, the Pareto optimal point has a minimum CRB of $0.1 \times 10^{-4} \text{ rad}^2$ and a rate of 2.044 kbps; at 120 m, it shifts to $0.6 \times 10^{-4} \text{ rad}^2$ with 2.045 kbps. For 140 m, the CRB rises to $1.5 \times 10^{-4} \text{ rad}^2$ and rate to 2.047 kbps, and at 160 m, the CRB reaches $3.5 \times 10^{-4} \text{ rad}^2$ with a rate of 2.047 kbps.

In contrast, when the target is closer to the BS, the CRB decreases as the BS transmit power dominates, improving the sensing performance despite the reduced user-target distance. However, with an overly dominant BS power, HRF gains become marginal. Thus, a trade-off exists between the echo power and reflected signal power at the BS, significantly

influencing HRF gains, as noted in [24].

3) Minimum number of bits required

Fig. 4c illustrates the minimum number of bits required by the ADC based on the DR of the UL signal received at the DFRC BS. This plot is generated by placing the target at random locations within a radius of 200 m from the BS while fixing the user at 100 m from the BS. At each location, the DR of the UL signal received at the BS is calculated using (34), along with the minimum ADC resolution necessary to observe the HRF phenomenon. The results indicate that the minimum required ADC resolution increases as the DR of the UL signal received at the BS increases, highlighting the relationship between signal DR and the ADC resolution needed to perform HRF effectively.

Note: For subsequent analyses, where various system parameters are varied to study their impact on the CRB-rate boundary of the HRF, we have assumed that the UL signal falls within the DR of the ADC. The results have been generated considering a 1-bit ADC, which introduces the maximum quantization distortion, thereby representing the minimum achievable performance. This provides a helpful benchmark for comparing and evaluating the effects of other system parameters in further analyses.

4) Impact of BS antenna array size

In Fig. 5, with settings $P = 1$, $K = 1$, $P^{\text{BS}} = 17$ dBm, $P_u = 20$ dBm, $N_k^u = 4$, and an AoA of $\theta = 30^\circ$, increasing the number of BS antennas (N) consistently improves performance, reducing CRB and increasing achievable rate. For $K = 1$, increasing N from 4 to 16 reduces the CRB from $1.1 \times 10^{-2} \text{ rad}^2$ to $3.9 \times 10^{-5} \text{ rad}^2$, while the rate improves from 0.2 kbps to 3.2 kbps. The Pareto optimal point also shifts: for $K = 1$ and $N = 4$, it is at a CRB of $1.12 \times 10^{-2} \text{ rad}^2$ with a rate of 0.1 kbps, improving to $4 \times 10^{-5} \text{ rad}^2$ with 2.2 kbps when $N = 16$. This trend holds for $K = 4$ and $K = 8$, showing that larger arrays benefit CRB and rate.

The monostatic case ($K = 0$) serves as a baseline. With $K = 0$ and $N = 4$, the CRB is $1.6 \times 10^{-2} \text{ rad}^2$, improving to $1.1 \times 10^{-2} \text{ rad}^2$ with one user ($K = 1$). The gains are more pronounced with more users; for $K = 8$ and $N = 4$, the CRB drops from $1.6 \times 10^{-2} \text{ rad}^2$ (for $K = 0$) to $0.4 \times 10^{-2} \text{ rad}^2$, a fourfold improvement, with similar trends across all N and K configurations.

These gains are mainly due to the increased array gain

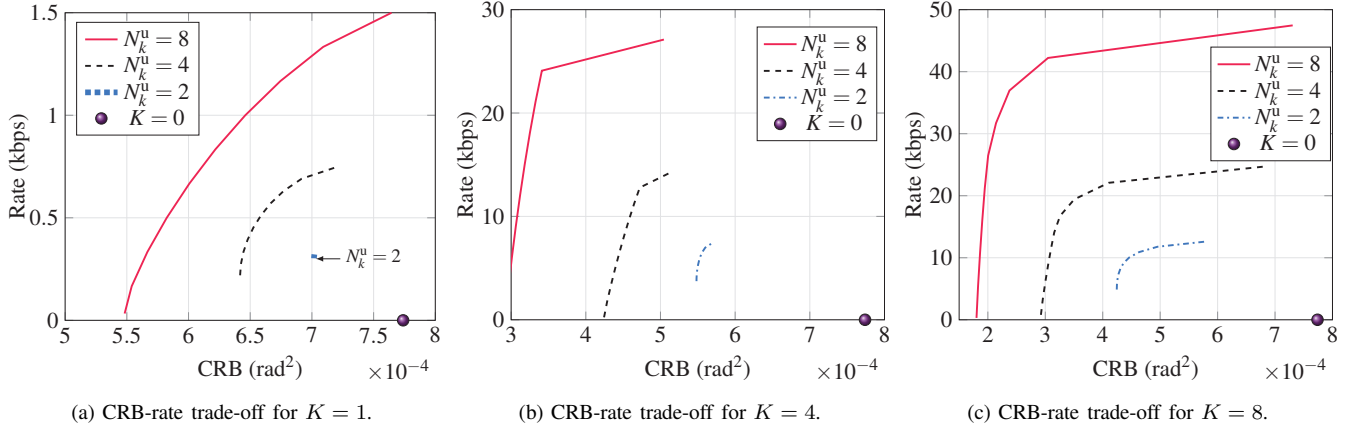


Fig. 6: CRB-rate trade-off for different numbers of users with varying user antenna array sizes.

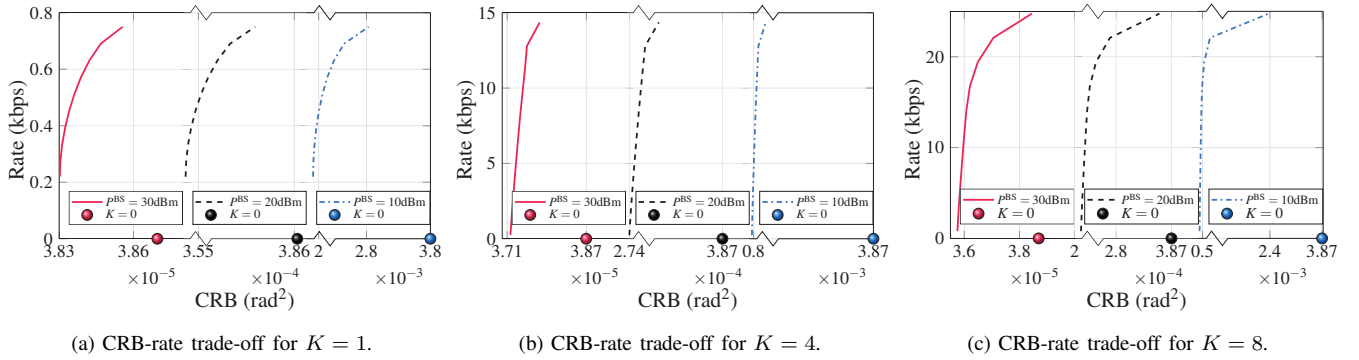


Fig. 7: CRB-rate trade-off for different numbers of users with varying BS transmit power.

from more antennas, which enhances SNR, improves AoA estimation accuracy, lowers CRB, and increases rates. As K increases, the CRB decreases further, reflecting the benefit of additional time samples. The CRB-rate boundary expands with more users, achieving lower CRB and higher rates. For $K = 4$ and $N = 8$, the boundary ranges from $4.2 \times 10^{-4} \text{ rad}^2$ to $5.2 \times 10^{-4} \text{ rad}^2$. Furthermore, increasing users to $K = 8$ broadens the boundary from 3×10^{-4} to $7.6 \times 10^{-4} \text{ rad}^2$, with the maximum rate rising from 15 kbps to 22 kbps.

5) Impact of user antenna array

The plots in Fig. 6 demonstrate the impact of increasing user transmit antennas (N_k^u) on HRF performance, using parameters from Section VI-B4 with $N = 8$. Results indicate that higher user antenna counts improve both CRB and rate across all configurations, mainly due to enhanced array gain that raises the SNR of the transmitted signal, improving both communication rate and AoA estimation accuracy.

For $K = 1$, increasing N_k^u from 2 to 8 reduces the CRB from approximately $7 \times 10^{-4} \text{ rad}^2$ to $5.5 \times 10^{-4} \text{ rad}^2$, while the rate increases from 0.4 kbps to 1.5 kbps. The CRB-rate boundary also widens with higher N_k^u and K . For $K = 1$ and $N_k^u = 2$, the boundary is near-singular, showing limited flexibility in balancing sensing and communication. However, for $K = 1$ and $N_k^u = 8$, the boundary broadens from $5.5 \times 10^{-4} \text{ rad}^2$ to $7.6 \times 10^{-4} \text{ rad}^2$, with rates between 0.1 kbps and 1.5 kbps. Similarly, for $K = 8$ and $N_k^u = 2$, the boundary spans from $4.2 \times 10^{-4} \text{ rad}^2$ to $5.8 \times 10^{-4} \text{ rad}^2$ with rates between 0.5 kbps and 12 kbps. Thus, increasing either

K or N_k^u consistently expands the CRB-rate boundary.

The Pareto optimal points also improve with higher N_k^u . For example, with $K = 8$ and $N_k^u = 2$, the optimal CRB-rate point is at $4.6 \times 10^{-4} \text{ rad}^2$ and 11 kbps. When N_k^u increases to 8, this point shifts to a CRB of $2.5 \times 10^{-4} \text{ rad}^2$ with a rate of 38 kbps. Similar trends are observed for $K = 4$ and $K = 1$.

In the monostatic case ($K = 0$), the CRB is $7.7 \times 10^{-4} \text{ rad}^2$, improving to $7 \times 10^{-4} \text{ rad}^2$ with the addition of one user ($K = 1$) and $N_k^u = 2$. As users increase, gains become more pronounced; with $K = 8$ and $N_k^u = 2$, the CRB drops from $7.7 \times 10^{-4} \text{ rad}^2$ (for $K = 0$) to $4.2 \times 10^{-4} \text{ rad}^2$, representing a 45% improvement. Similar enhancements are seen across all configurations of N_k^u and K .

6) Impact of BS transmit power

The plots in Fig. 7 show the effect of varying BS transmit power (P^{BS}) on the CRB-rate trade-off across user scenarios, using parameters from Section VI-B4 with $N = 8$. For $K = 1$, at $P^{\text{BS}} = 30 \text{ dBm}$, the minimum CRB along the CRB-rate boundary is approximately $3.83 \times 10^{-5} \text{ rad}^2$. Reducing P^{BS} to 20 dBm increases this CRB to $3.5 \times 10^{-4} \text{ rad}^2$, and at 10 dBm, it rises to $1.9 \times 10^{-3} \text{ rad}^2$. Notably, the rate remains constant at 0.2 kbps, showing that while increased P^{BS} lowers the CRB by enhancing the SNR of reflected signals, it does not impact the uplink signals driving communication rate.

Only the CRB of Pareto optimal points varies with P^{BS} . For $K = 1$ at $P^{\text{BS}} = 10 \text{ dBm}$, the CRB is $2 \times 10^{-3} \text{ rad}^2$, which improves to $3.83 \times 10^{-5} \text{ rad}^2$ at $P^{\text{BS}} = 30 \text{ dBm}$ —a 100-fold enhancement with a 20 dBm power increase.

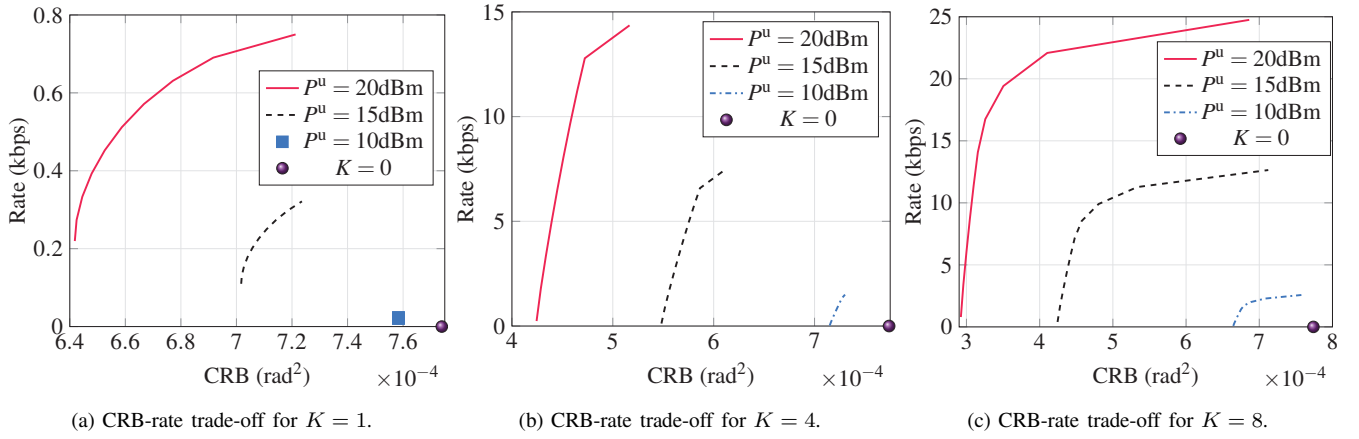


Fig. 8: CRB-rate trade-off for different numbers of users with varying user transmit power.

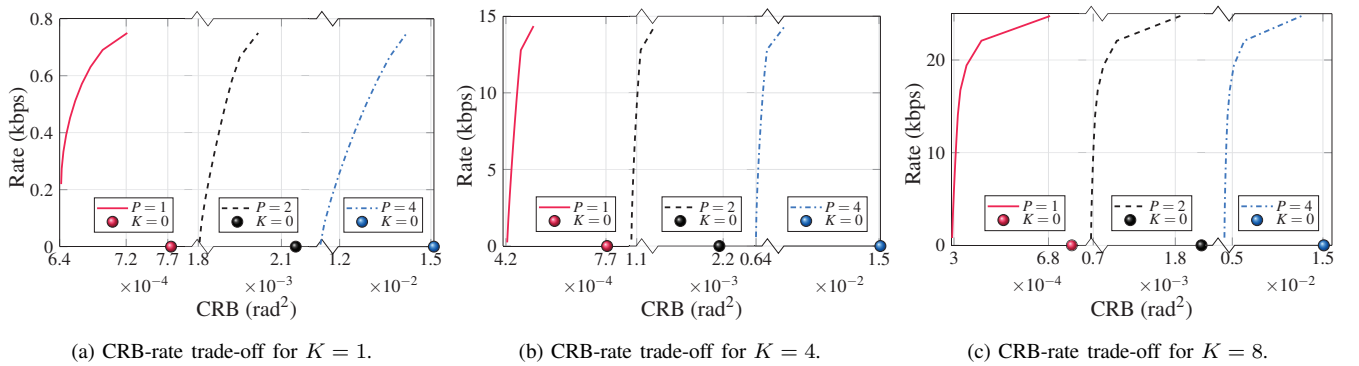


Fig. 9: CRB-rate trade-off for different numbers of users with varying numbers of targets in the scene.

In the monostatic case ($K = 0$) with $P^{\text{BS}} = 30$ dBm, the CRB is $3.87 \times 10^{-5} \text{rad}^2$. Adding users slightly improves the CRB: for $K = 1$, the CRB is $3.83 \times 10^{-5} \text{rad}^2$, and for $K = 8$, it further reduces to $3.58 \times 10^{-5} \text{rad}^2$. However, these improvements are modest compared to those achieved by increasing the number of BS and user antennas, suggesting that antenna configuration has a greater impact on performance than BS transmit power alone.

7) Impact of user transmit power

The plots in Fig. 8 illustrate how varying user transmit power (P^u) impacts the CRB-rate trade-off across user configurations, with parameters from Section VI-B4 and $N = 8$. Increasing P^u enhances both CRB and rate in all scenarios due to the improved SNR of uplink signals, which boosts sensing accuracy and communication rates.

For $K = 1$, raising P^u from 10 dBm to 20 dBm decreases the CRB from approximately $7.5 \times 10^{-4} \text{rad}^2$ to $6.4 \times 10^{-4} \text{rad}^2$, while the rate increases from 0.1 kbps to 0.8 kbps. The CRB-rate boundary also expands with higher P^u and K . For $K = 1$ and $P^u = 10$ dBm, the boundary is almost a single point, indicating limited flexibility in balancing sensing and communication. At $P^u = 20$ dBm, the boundary broadens from $6.4 \times 10^{-4} \text{rad}^2$ at 0.21 kbps to $7.21 \times 10^{-4} \text{rad}^2$ at 0.75 kbps. For $K = 8$ and $P^u = 10$ dBm, the CRB-rate boundary spans from $6.7 \times 10^{-4} \text{rad}^2$ to $7.6 \times 10^{-4} \text{rad}^2$ with rates from 0.5 kbps to 3 kbps, showing the advantage of higher power and user count.

The Pareto optimal points also improve with increasing P^u . For example, with $K = 8$ and $P^u = 10$ dBm, the Pareto optimal point achieves a CRB of $6.8 \times 10^{-4} \text{rad}^2$ at 2 kbps, which improves to $3.6 \times 10^{-4} \text{rad}^2$ at 21 kbps when P^u is raised to 20 dBm. Similar shifts occur for $K = 4$ and $K = 1$.

In the monostatic case ($K = 0$), the CRB is around $7.8 \times 10^{-4} \text{rad}^2$, improving slightly to $7.6 \times 10^{-4} \text{rad}^2$ with $K = 1$ and $P^u = 10$ dBm. As users increase, gains become more significant; with $K = 8$ and $P^u = 10$ dBm, the CRB drops from $7.8 \times 10^{-4} \text{rad}^2$ (monostatic) to $6.7 \times 10^{-4} \text{rad}^2$, marking a 37% improvement. These enhancements hold across all values of P^u and K .

8) Impact of the number of targets

The plots in Fig. 9 examine the CRB-rate trade-off as the number of targets (P) varies across user configurations, using the parameters in Section VI-B4 with $N = 8$. For $K = 1$, increasing targets from $P = 1$ to $P = 4$ raises the CRB from approximately $6.4 \times 10^{-4} \text{rad}^2$ to $1.1 \times 10^{-2} \text{rad}^2$. Similarly, in the $K = 4$ case, increasing P from 1 to 4 results in a CRB rise from $4.2 \times 10^{-4} \text{rad}^2$ to $0.64 \times 10^{-2} \text{rad}^2$. For $K = 8$, the CRB increases from approximately $3 \times 10^{-4} \text{rad}^2$ to $0.4 \times 10^{-2} \text{rad}^2$ as targets increase. The CRB rise across all user scenarios reflects the division of BS transmit power among more targets, reducing per-target SNR and, thus, AoA estimation accuracy.

Increasing the number of users (K) improves the CRB. For instance, in a monostatic configuration ($K = 0$) with $P = 1$, the CRB is $7.7 \times 10^{-4} \text{rad}^2$. Adding one user ($K = 1$)

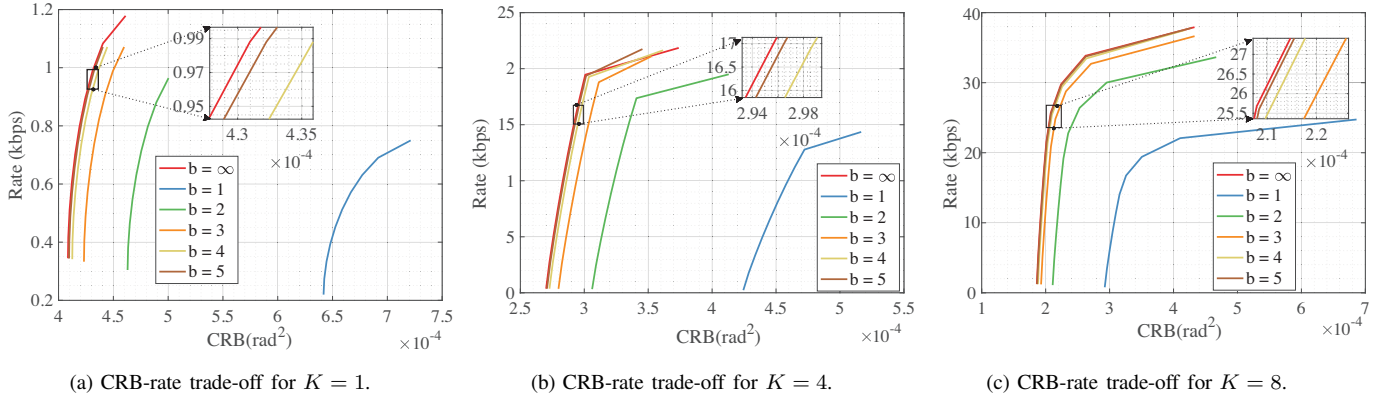


Fig. 10: CRB-rate trade-off for different numbers of users with varying ADC resolution.

reduces the CRB to $6.4 \times 10^{-4} \text{ rad}^2$ for $P = 1$, and further decreases occur as K increases. At $K = 8$ and $P = 1$, the CRB reaches $3 \times 10^{-4} \text{ rad}^2$, illustrating the benefit of multi-user configurations for enhanced sensing performance.

9) Impact of ADC Resolution

The plots in Fig. 10 show the CRB-rate trade-off as ADC resolution varies across user configurations, using parameters from Section VI-B4 with $N = 8$. For $K = 1$, increasing ADC resolution from $b = 1$ bit to $b = \infty$ (ideal resolution) reduces the minimum CRB from approximately $6.4 \times 10^{-4} \text{ rad}^2$ to $4.2 \times 10^{-4} \text{ rad}^2$ and raises the achievable rate from about 0.7 kbps to 1.2 kbps. Gains diminish beyond $b = 4$ bits, suggesting limited improvement in CRB and rate with further increases in ADC resolution. Similar trends appear for $K = 4$ and $K = 8$, with higher ADC resolution yielding better CRB and rate due to reduced quantization noise and improved SNR.

The Pareto optimal points also improve as ADC resolution increases. For instance, with $K = 8$ and $b = 1$ bit, the optimal point achieves a CRB of $3.9 \times 10^{-4} \text{ rad}^2$ at a rate of 21 kbps; increasing to $b = 3$ bits shifts this point to a CRB of $2.8 \times 10^{-4} \text{ rad}^2$ with a rate of 32 kbps. Gains taper off at resolutions above 4 bits, indicating diminishing returns. These findings suggest that while higher ADC resolutions reduce CRB and increase achievable rates, operating at a resolution that maintains acceptable distortion is more efficient, avoiding the power costs of higher resolutions for minimal performance gains.

VII. CONCLUSION AND RESEARCH DIRECTIONS

In this work, we have thoroughly investigated the performance limits of HRF systems, considering quantization effects caused by finite-resolution ADCs. Our analysis reveals that the DR of ADCs plays a crucial role in determining the CRB and communication rate trade-offs in HRF systems. We have derived the CRB for HRF considering finite-resolution ADCs. We have also derived lower bounds on both the FIM and UL communication rates, which are used in the study of the limits of HRF. We have proposed two optimization problems to quantify the CRB-rate boundaries of the HRF system. The results highlight that increasing the ADC resolution enhances the system's ability to distinguish between direct and reflected signals, improving sensing accuracy and communication quality. Furthermore, we have identified key

trade-offs in CRB-rate performance across varying system parameters, such as target distance and antenna array size, BS transmit power, and user transmit power. These trade-offs play a crucial role in choosing the necessary parameters for HRF. Our future work will focus on developing receive beamforming techniques aimed at mitigating the dynamic range limitations of ADCs. By reducing the dynamic range of the UL signal through targeted receive processing, we aim to lower the required ADC resolution, thus further optimizing the overall system performance in HRF applications. This approach lays the groundwork for more advanced ISAC systems, where communication and sensing tasks can be balanced effectively, even under stringent hardware constraints.

APPENDIX A

PARTIAL DERIVATIVES OF $x_{n,\ell}$ WITH ALL UNKNOWN PARAMETERS

The partial derivatives of $x_{n,\ell}$ w.r.t all the sensing parameters of interest are as follows

$$\begin{aligned} \frac{\partial x_{n,\ell}}{\partial \theta_i^{\text{tar}}} &= \sum_{m_1 \in \mathcal{C}_0} b_{m_1,0}^\ell \tilde{\gamma}_{i,\ell}^{\text{tar}} c_{m_1}(2\tau_i^{\text{tar}}, v) (\dot{a}_{n,r}(\theta_i^{\text{tar}}) \mathbf{a}_t^{\text{T}}(\theta_i^{\text{tar}}) \\ &+ a_{n,r}(\theta_i^{\text{tar}}) \mathbf{a}_t^{\text{T}}(\theta_i^{\text{tar}})) \mathbf{f} + \sum_{\substack{k=1 \\ m_2 \in \mathcal{C}_k}}^K b_{m_2,k}^\ell \tilde{\gamma}_{k,i,\ell}^{\text{tar}} \\ &c_{m_2}(\phi_{k,i}, v) \dot{a}_{n,r}(\theta_i^{\text{tar}}) (\mathbf{a}_{k,t}^{\text{u}}(\theta_{k,i}^{\text{u}}))^{\text{T}} \mathbf{f}_k^{\text{u}}, \end{aligned} \quad (35)$$

$$\begin{aligned} \frac{\partial x_{n,\ell}}{\partial f_{D,i}} &= \sum_{m_1 \in \mathcal{C}_0} b_{m_1,0}^\ell \tilde{\gamma}_{i,\ell}^{\text{tar}} j 2\pi \ell T c_{m_1}(2\tau_i^{\text{tar}}, v) a_{n,r}(\theta_i^{\text{tar}}) \\ &\mathbf{a}_t^{\text{T}}(\theta_i^{\text{tar}}) \mathbf{f} + \sum_{\substack{k=1 \\ m_2 \in \mathcal{C}_k}}^K b_{m_2,k}^\ell \tilde{\gamma}_{k,i,\ell}^{\text{tar}} j 2\pi \ell T c_{m_2}(\phi_{k,i}, v) a_{n,r}(\theta_i^{\text{tar}}) \\ &(\mathbf{a}_{k,t}^{\text{u}}(\theta_{k,i}^{\text{u}}))^{\text{T}} \mathbf{f}_k^{\text{u}}, \end{aligned} \quad (36)$$

$$\begin{aligned} \frac{\partial x_{n,\ell}}{\partial \tau_i^{\text{tar}}} &= \sum_{m_1 \in \mathcal{C}_0} b_{m_1,0}^\ell \tilde{\gamma}_{i,\ell}^{\text{tar}} (-j 4\pi(m_1 \Delta f + f_c)) c_{m_1}(2\tau_i^{\text{tar}}, v) \\ &a_{n,r}(\theta_i^{\text{tar}}) \mathbf{a}_t^{\text{T}}(\theta_i^{\text{tar}}) \mathbf{f}, \\ \frac{\partial x_{n,\ell}}{\partial \theta_{r,k}^{\text{u}}} &= \sum_{m_2 \in \mathcal{C}_k} b_{m_2,k}^\ell g_{k,0}^{\text{u}} c_{m_2}(\tau_k^{\text{u}}, v) \dot{a}_{n,r}(\theta_{r,k}^{\text{u}}) (\mathbf{a}_{k,t}^{\text{u}}(\theta_k^{\text{u}}))^{\text{T}} \mathbf{f}_k^{\text{u}}, \\ \frac{\partial x_{n,\ell}}{\partial \theta_k^{\text{u}}} &= \sum_{m_2 \in \mathcal{C}_k} b_{m_2,k}^\ell g_{k,0}^{\text{u}} c_{m_2}(\tau_k^{\text{u}}, v) a_{n,r}(\theta_{r,k}^{\text{u}}) (\mathbf{a}_{k,t}^{\text{u}}(\theta_k^{\text{u}}))^{\text{T}} \mathbf{f}_k^{\text{u}}, \end{aligned}$$

$$\begin{aligned} \frac{\partial x_{n,\ell}}{\partial \tau_k^u} &= \sum_{m_2 \in \mathcal{C}_k} b_{m_2,k}^\ell g_{k,0}^u (-j2\pi(m_2\Delta_f + f_c)) c_{m_2}(\tau_k^u, v) \\ & a_{n,r}(\theta_{r,k}^u) (\mathbf{a}_{k,t}^u(\theta_{k,j}^u))^T \mathbf{f}_{k,t}^u, \\ \frac{\partial x_{n,\ell}}{\partial \phi_{k,j}} &= \sum_{m_2 \in \mathcal{C}_k} b_{m_2,k}^\ell \tilde{\gamma}_{k,i,\ell}^{\text{tar}} (-j2\pi(m_2\Delta_f + f_c)) c_{m_2}(\phi_{k,j}, v) \\ & a_{n,r}(\theta_j^{\text{tar}}) (\mathbf{a}_{k,t}^u(\theta_{k,j}^u))^T \mathbf{f}_{k,t}^u, \\ \frac{\partial x_{n,\ell}}{\partial \theta_{k,j}^u} &= \sum_{m_2 \in \mathcal{C}_k} b_{m_2,k}^\ell \tilde{\gamma}_{k,i,\ell}^{\text{tar}} c_{m_2}(\phi_{k,j}, v) a_{n,r}(\theta_j^{\text{tar}}) \\ & (\mathbf{a}_{k,t}^u(\theta_{k,j}^u))^T \mathbf{f}_{k,t}^u, \\ \frac{\partial x_{n,\ell}}{\partial g_i^{\text{R,tar}}} &= \sum_{m_1 \in \mathcal{C}_0} b_{m_1,0}^\ell e^{j2\pi f_{D,i} \ell T} c_{m_1}(2\tau_i^{\text{tar}}, v) a_{n,r}(\theta_i^{\text{tar}}) \\ & \mathbf{a}_t^T(\theta_i^{\text{tar}}) \mathbf{f}, \\ \frac{\partial x_{n,\ell}}{\partial g_i^{\text{I,tar}}} &= \sum_{m_1 \in \mathcal{C}_0} j b_{m_1,0}^\ell e^{j2\pi f_{D,i} \ell T} c_{m_1}(2\tau_i^{\text{tar}}, v) a_{n,r}(\theta_i^{\text{tar}}) \\ & \mathbf{a}_t^T(\theta_i^{\text{tar}}) \mathbf{f}, \\ \frac{\partial x_{n,\ell}}{\partial g_{k,0}^{\text{R,u}}} &= \sum_{m_2 \in \mathcal{C}_k} b_{m_2,k}^\ell c_{m_2}(\tau_k^u, v) a_{n,r}(\theta_{r,k}^u) (\mathbf{a}_{k,t}^u(\theta_{k,j}^u))^T \mathbf{f}_{k,t}^u, \\ \frac{\partial x_{n,\ell}}{\partial g_{k,0}^{\text{I,u}}} &= \sum_{m_2 \in \mathcal{C}_k} j b_{m_2,k}^\ell c_{m_2}(\tau_k^u, v) a_{n,r}(\theta_{r,k}^u) (\mathbf{a}_{k,t}^u(\theta_{k,j}^u))^T \mathbf{f}_{k,t}^u, \\ \frac{\partial x_{n,\ell}}{\partial g_{k,j}^{\text{R,u}}} &= \sum_{m_2 \in \mathcal{C}_k} b_{m_2,k}^\ell e^{j2\pi f_{D,j} \ell T} c_{m_2}(\phi_{k,j}, v) a_{n,r}(\theta_j^{\text{tar}}) \\ & (\mathbf{a}_{k,t}^u(\theta_{k,j}^u))^T \mathbf{f}_{k,t}^u, \\ \frac{\partial x_{n,\ell}}{\partial g_{k,j}^{\text{I,u}}} &= \sum_{m_2 \in \mathcal{C}_k} j b_{m_2,k}^\ell e^{j2\pi f_{D,j} \ell T} c_{m_2}(\phi_{k,j}, v) a_{n,r}(\theta_j^{\text{tar}}) \\ & (\mathbf{a}_{k,t}^u(\theta_{k,j}^u))^T \mathbf{f}_{k,t}^u. \end{aligned}$$

APPENDIX B

DERIVATION OF COVARIANCE MATRIX $\mathbf{R}_{\mathbf{x}_\ell \mathbf{x}_\ell}$

The covariance matrix $\mathbf{R}_{\mathbf{x}_\ell \mathbf{x}_\ell}$ is given as $\mathbf{R}_{\mathbf{x}_\ell \mathbf{x}_\ell} = \mathbb{E} \{ \mathbf{x}_\ell \mathbf{x}_\ell^H \}$. Using (5), we get each term separately as follows $\mathbf{x}_\ell^{\text{echo}} = \sum_{m \in \mathcal{C}_0} b_{m,0}^\ell \mathbf{H}_{\ell,m,i}^{\text{echo}} \mathbf{f}$, $\mathbf{x}_\ell^{\text{dp}} = \sum_{m \in \mathcal{C}_k} b_{m,k}^\ell \mathbf{H}_{\ell,m,k}^{\text{dp}} \mathbf{f}_k^u$, and $\mathbf{x}_\ell^{\text{ref}} = \sum_{m \in \mathcal{C}_k} \sum_{j \in \Phi_k} b_{m,k}^\ell \mathbf{H}_{\ell,m,k,j}^{\text{ref}} \mathbf{f}_k^u$. Thus, we can rewrite \mathbf{x}_ℓ as $\mathbf{x}_\ell = \mathbf{x}_\ell^{\text{echo}} + \mathbf{x}_\ell^{\text{dp}} + \mathbf{x}_\ell^{\text{ref}}$. Now, the covariance matrix $\mathbf{R}_{\mathbf{x}_\ell \mathbf{x}_\ell}$ can be expanded as

$$\mathbf{R}_{\mathbf{x}_\ell \mathbf{x}_\ell} = \mathbb{E} \left\{ \left(\mathbf{x}_\ell^{\text{echo}} + \mathbf{x}_\ell^{\text{dp}} + \mathbf{x}_\ell^{\text{ref}} \right) \left(\mathbf{x}_\ell^{\text{echo}} + \mathbf{x}_\ell^{\text{dp}} + \mathbf{x}_\ell^{\text{ref}} \right)^H \right\}. \quad (37)$$

Expanding the expectation, we get

$$\mathbf{R}_{\mathbf{x}_\ell \mathbf{x}_\ell} = \mathbf{R}_{\mathbf{x}_\ell^{\text{echo}} \mathbf{x}_\ell^{\text{echo}}} + \mathbf{R}_{\mathbf{x}_\ell^{\text{dp}} \mathbf{x}_\ell^{\text{dp}}} + \mathbf{R}_{\mathbf{x}_\ell^{\text{ref}} \mathbf{x}_\ell^{\text{ref}}} + \mathbf{R}_{\mathbf{x}_\ell^{\text{echo}} \mathbf{x}_\ell^{\text{dp}}} \quad (38)$$

+ $\mathbf{R}_{\mathbf{x}_\ell^{\text{dp}} \mathbf{x}_\ell^{\text{echo}}}$ + $\mathbf{R}_{\mathbf{x}_\ell^{\text{echo}} \mathbf{x}_\ell^{\text{ref}}}$ + $\mathbf{R}_{\mathbf{x}_\ell^{\text{ref}} \mathbf{x}_\ell^{\text{echo}}}$ + $\mathbf{R}_{\mathbf{x}_\ell^{\text{dp}} \mathbf{x}_\ell^{\text{ref}}}$ + $\mathbf{R}_{\mathbf{x}_\ell^{\text{ref}} \mathbf{x}_\ell^{\text{dp}}}$, where $\mathbf{R}_{\mathbf{x}_\ell^{\text{echo}} \mathbf{x}_\ell^{\text{echo}}}$, $\mathbf{R}_{\mathbf{x}_\ell^{\text{dp}} \mathbf{x}_\ell^{\text{dp}}}$, and $\mathbf{R}_{\mathbf{x}_\ell^{\text{ref}} \mathbf{x}_\ell^{\text{ref}}}$ are the covariance matrices of the echo, direct path, and reflection components, respectively. $\mathbf{R}_{\mathbf{x}_\ell^{\text{echo}} \mathbf{x}_\ell^{\text{dp}}}$, $\mathbf{R}_{\mathbf{x}_\ell^{\text{dp}} \mathbf{x}_\ell^{\text{echo}}}$, $\mathbf{R}_{\mathbf{x}_\ell^{\text{echo}} \mathbf{x}_\ell^{\text{ref}}}$, $\mathbf{R}_{\mathbf{x}_\ell^{\text{ref}} \mathbf{x}_\ell^{\text{echo}}}$, $\mathbf{R}_{\mathbf{x}_\ell^{\text{dp}} \mathbf{x}_\ell^{\text{ref}}}$, and $\mathbf{R}_{\mathbf{x}_\ell^{\text{ref}} \mathbf{x}_\ell^{\text{dp}}}$ represent the cross-covariances between the echo, direct path, and reflection components in pairs. We make the following assumption to simplify the terms

$$\mathbb{E} \left[b_{m_1,k_1}^{(\ell)*} b_{m_2,k_2}^{(\ell)} \right] = \sigma_{k_1}^2 \delta_{m_1,m_2} \delta_{k_1,k_2}. \quad (39)$$

Evaluating individual terms and using the assumption, we get

$$\mathbf{R}_{\mathbf{x}_\ell^{\text{echo}} \mathbf{x}_\ell^{\text{echo}}} = \sigma_0^2 \sum_{i \in \Phi_0} \mathbf{H}_{\ell,m,i}^{\text{echo}} \mathbf{R}_f \left(\mathbf{H}_{\ell,m,i}^{\text{echo}} \right)^H, \quad (40)$$

$$\mathbf{R}_{\mathbf{x}_\ell^{\text{dp}} \mathbf{x}_\ell^{\text{dp}}} = \sum_{k=1}^K \sigma_k^2 \mathbf{H}_{\ell,m,k}^{\text{dp}} \mathbf{R}_{\mathbf{f}_k^u} \left(\mathbf{H}_{\ell,m,k}^{\text{dp}} \right)^H, \quad (41)$$

$$\mathbf{R}_{\mathbf{x}_\ell^{\text{ref}} \mathbf{x}_\ell^{\text{ref}}} = \sum_{m \in \mathcal{C}_k} \sum_{k=1}^K \sum_{j \in \Phi_k} \sigma_k^2 \mathbf{H}_{\ell,m,k,j}^{\text{ref}} \mathbf{R}_{\mathbf{f}_k^u} \left(\mathbf{H}_{\ell,m,k,j}^{\text{ref}} \right)^H. \quad (42)$$

From (39), $\mathbb{E} \left\{ \mathbf{x}_\ell^{\text{echo}} \left(\mathbf{x}_\ell^{\text{dp}} \right)^H \right\} = 0$, $\mathbb{E} \left\{ \mathbf{x}_\ell^{\text{dp}} \left(\mathbf{x}_\ell^{\text{echo}} \right)^H \right\} = 0$, $\mathbb{E} \left\{ \mathbf{x}_\ell^{\text{echo}} \left(\mathbf{x}_\ell^{\text{ref}} \right)^H \right\} = 0$, and $\mathbb{E} \left\{ \mathbf{x}_\ell^{\text{ref}} \left(\mathbf{x}_\ell^{\text{echo}} \right)^H \right\} = 0$. Evaluating $\mathbb{E} \left\{ \mathbf{x}_\ell^{\text{dp}} \left(\mathbf{x}_\ell^{\text{ref}} \right)^H \right\}$ and using (39), we get,

$$\begin{aligned} \mathbf{R}_{\mathbf{x}_\ell^{\text{dp}} \mathbf{x}_\ell^{\text{ref}}} &= \sum_{k=1}^K \sum_{m \in \mathcal{C}_k} \sum_{j \in \Phi_k} \sigma_k^2 \mathbf{H}_{\ell,m,k}^{\text{dp}} \mathbf{R}_{\mathbf{f}_k^u} \left(\mathbf{H}_{\ell,m,k,j}^{\text{ref}} \mathbf{f}_k^u \right)^H \\ &= \sum_{k=1}^K \sum_{m \in \mathcal{C}_k} \sum_{j \in \Phi_k} \sigma_k^2 \mathbf{H}_{\ell,m,k}^{\text{dp}} \mathbf{R}_{\mathbf{f}_k^u} \left(\mathbf{H}_{\ell,m,k,j}^{\text{ref}} \right)^H. \end{aligned} \quad (43)$$

Similarly,

$$\mathbf{R}_{\mathbf{x}_\ell^{\text{ref}} \mathbf{x}_\ell^{\text{dp}}} = \sum_{k=1}^K \sum_{m \in \mathcal{C}_k} \sum_{j \in \Phi_k} \sigma_k^2 \mathbf{H}_{\ell,m,k,j}^{\text{ref}} \mathbf{R}_{\mathbf{f}_k^u} \left(\mathbf{H}_{\ell,m,k}^{\text{dp}} \right)^H. \quad (44)$$

Combining all the results, we get

$$\begin{aligned} \mathbf{R}_{\mathbf{x}_\ell \mathbf{x}_\ell} &= \sum_{k=1}^K \sigma_k^2 \mathbf{H}_{\ell,m,k}^{\text{dp}} \mathbf{R}_{\mathbf{f}_k^u} \left(\mathbf{H}_{\ell,m,k}^{\text{dp}} \right)^H \\ &+ \sum_{k=1}^K \sum_{m \in \mathcal{C}_k} \sum_{j \in \Phi_k} \sum_{p \in \Phi_k} \sigma_k^2 \mathbf{H}_{\ell,m,k,j}^{\text{ref}} \mathbf{R}_{\mathbf{f}_k^u} \left(\mathbf{H}_{\ell,m,k,p}^{\text{ref}} \right)^H \\ &+ \sum_{k=1}^K \sum_{m \in \mathcal{C}_k} \sum_{j \in \Phi_k} \sigma_k^2 \mathbf{H}_{\ell,m,k}^{\text{dp}} \mathbf{R}_{\mathbf{f}_k^u} \left(\mathbf{H}_{\ell,m,k,j}^{\text{ref}} \right)^H \\ &+ \sum_{k=1}^K \sum_{m \in \mathcal{C}_k} \sum_{j \in \Phi_k} \sigma_k^2 \mathbf{H}_{\ell,m,k,j}^{\text{ref}} \mathbf{R}_{\mathbf{f}_k^u} \left(\mathbf{H}_{\ell,m,k}^{\text{dp}} \right)^H \end{aligned} \quad (45)$$

APPENDIX C

DERIVATION OF FIM OF AOA OF TARGETS AT LOW SNR

We here evaluate (22) for $\psi_i = \theta_i^{\text{tar}}$ and $\psi_j = \theta_j^{\text{tar}}$. A similar procedure and assumptions can be followed for deriving the expressions for other parameters of interest.

$$\begin{aligned} \left(\frac{\partial x_{n,\ell}}{\partial \theta_i^{\text{tar}}} \right)^* \frac{\partial x_{n,\ell}}{\partial \theta_j^{\text{tar}}} &= \left(\sum_{m_1 \in \mathcal{C}_0} b_{m_1,0}^{(\ell)} \mathbf{A}_{n,\ell,m_1}^{i,v} \mathbf{f} + \sum_{k_1=1}^K \sum_{m_2 \in \mathcal{C}_{k_1}} b_{m_2,k_1}^{(\ell)} \mathbf{B}_{n,\ell,m_2}^{k_1,i,v} \mathbf{f}_{k_1}^u \right)^* \\ & \left(\sum_{m'_1 \in \mathcal{C}_0} b_{m'_1,0}^{(\ell)} \mathbf{A}_{n,\ell,m'_1}^{j,v} \mathbf{f} + \sum_{k_2=1}^K \sum_{m'_2 \in \mathcal{C}_{k_2}} b_{m'_2,k_2}^{(\ell)} \mathbf{B}_{n,\ell,m'_2}^{k_2,j,v} \mathbf{f}_{k_2}^u \right), \end{aligned} \quad (46)$$

where

$$\begin{aligned} \mathbf{A}_{n,\ell,m_1}^{i,v} &= \tilde{\gamma}_{i,\ell}^{\text{tar}} c_{m_1}(2\tau_i^{\text{tar}}, v) \left(\dot{a}_{n,r}(\theta_i^{\text{tar}}) \mathbf{a}_t^T(\theta_i^{\text{tar}}) \right. \\ & \left. + a_{n,r}(\theta_i^{\text{tar}}) \dot{\mathbf{a}}_t^T(\theta_i^{\text{tar}}) \right), \end{aligned} \quad (47)$$

$$\mathbf{B}_{n,\ell,m_2}^{k_1,i,v} = \tilde{\gamma}_{k_1,i,\ell}^{\text{tar}} c_{m_2}(\phi_{k_1,i}, v) \dot{a}_{n,r}(\theta_i^{\text{tar}}) \left(\mathbf{a}_{k_1,t}^u(\theta_{k_1,i}^u) \right)^T \quad (48)$$

Using (39) and collecting a large number of samples for estimation, we can write (46) as

$$\begin{aligned} \left(\frac{\partial x_{n,\ell}}{\partial \theta_i^{\text{tar}}} \right)^* \frac{\partial x_{n,\ell}}{\partial \theta_j^{\text{tar}}} &= \sigma_0^2 \sum_{m_1 \in \mathcal{C}_0} \text{tr} \left(\mathbf{f}^H \left(\mathbf{A}_{n,\ell,m_1}^{i,v} \right)^H \mathbf{A}_{n,\ell,m_1}^{j,v} \right) \\ &+ \sum_{k=1}^K \sum_{m_2 \in \mathcal{C}_k} \sigma_k^2 \text{tr} \left(\mathbf{f}_k^u \left(\mathbf{f}_k^u \right)^H \left(\mathbf{B}_{n,\ell,m_2}^{k,i,v} \right)^H \mathbf{B}_{n,\ell,m_2}^{k,j,v} \right). \end{aligned} \quad (49)$$

Replacing $\mathbf{f}^H = \mathbf{R}_0$ and $\mathbf{f}_k^u \left(\mathbf{f}_k^u \right)^H = \mathbf{R}_k$ and adding over NL samples, we get

$$\begin{aligned} \left(\frac{\partial \mathbf{x}}{\partial \theta_i^{\text{tar}}} \right)^H \frac{\partial \mathbf{x}}{\partial \theta_j^{\text{tar}}} &= \sum_{n=1}^N \sum_{\ell=1}^L \left[\sigma_0^2 \sum_{m_1 \in \mathcal{C}_0} \text{tr} \left(\mathbf{R}_0 \left(\mathbf{A}_{n,\ell,m_1}^{i,v} \right)^H \mathbf{A}_{n,\ell,m_1}^{j,v} \right) \right. \end{aligned}$$

$$+ \sum_{\substack{k=1 \\ m_2 \in \mathcal{C}_k}}^K \sigma_k^2 \sum \text{tr} \left(\mathbf{R}_k \left(\mathbf{B}_{n,\ell,m_2}^{k,i,v} \right)^H \mathbf{B}_{n,\ell,m_2}^{k,j,v} \right) \right]. \quad (50)$$

Finally, the lower bound on the FIM of Θ is given as

$$\begin{aligned} \left[\mathbf{F}_{\text{FIM}}^{\text{LS}}(\Theta) \right]_{ij} = & \frac{2(1-\eta)}{\sigma^2} \Re \left[\sum_{n=1}^N \sum_{\ell=1}^L \left(\sigma_0^2 \sum_{m_1 \in \mathcal{C}_0} \text{tr} \left(\mathbf{R}_0 \left(\mathbf{A}_{n,\ell,m_1}^{i,v} \right)^H \mathbf{A}_{n,\ell,m_1}^{j,v} \right) \right) \right. \\ & \left. + \sum_{\substack{k=1 \\ m_2 \in \mathcal{C}_k}}^K \sigma_k^2 \text{tr} \left(\mathbf{R}_k \left(\mathbf{B}_{n,\ell,m_2}^{k,i,v} \right)^H \mathbf{B}_{n,\ell,m_2}^{k,j,v} \right) \right) \right]. \quad (51) \end{aligned}$$

REFERENCES

- [1] M. Chafii, L. Bariah, S. Muhaidat, and M. Debbah, "Twelve Scientific Challenges for 6G: Rethinking the Foundations of Communications Theory," *IEEE Communications Surveys & Tutorials*, vol. 25, no. 2, pp. 868–904, 2023.
- [2] International Telecommunication Union, "Framework and overall objectives of the future development of IMT for 2030 and beyond," Geneva, Switzerland, Tech. Rep. ITU-R M.2160-0, Nov 2023. [Online]. Available: https://www.itu.int/dms_pubrec/itu-r/rec/m/R-REC-M.2160-0-202311-1!!!PDF-E.pdf
- [3] A. Bazzi and M. Chafii, "On Outage-Based Beamforming Design for Dual-Functional Radar-Communication 6G Systems," *IEEE Transactions on Wireless Communications*, vol. 22, no. 8, pp. 5598–5612, 2023.
- [4] A. Bazzi and M. Chafii, "On Integrated Sensing and Communication Waveforms With Tunable PAPR," *IEEE Transactions on Wireless Communications*, vol. 22, no. 11, pp. 7345–7360, 2023.
- [5] F. Liu, L. Zhou, C. Masouros, A. Li, W. Luo, and A. Petropulu, "Toward Dual-functional Radar-Communication Systems: Optimal Waveform Design," *IEEE Transactions on Signal Processing*, vol. 66, no. 16, pp. 4264–4279, Aug. 2018.
- [6] F. Liu, L. Zheng, Y. Cui, C. Masouros, A. P. Petropulu, H. Griffiths, and Y. C. Eldar, "Seventy Years of Radar and Communications: The road from separation to integration," *IEEE Signal Processing Magazine*, vol. 40, no. 5, pp. 106–121, Jul. 2023.
- [7] A. Bazzi and M. Chafii, "Secure Full Duplex Integrated Sensing and Communications," *IEEE Transactions on Information Forensics and Security*, vol. 19, pp. 2082–2097, 2024.
- [8] S. Dutta, C. N. Barati, D. Ramirez, A. Dhananjay, J. F. Buckwalter, and S. Rangan, "A Case for Digital Beamforming at mmWave," *IEEE Transactions on Wireless Communications*, vol. 19, no. 2, pp. 756–770, Feb. 2020.
- [9] R. W. Heath, N. Gonzalez-Prelcic, S. Rangan, W. Roh, and A. M. Sayeed, "An Overview of Signal Processing Techniques for Millimeter Wave MIMO Systems," *IEEE Journal of Selected Topics in Signal Processing*, vol. 10, no. 3, pp. 436–453, Apr. 2016.
- [10] R. Walden, "Analog-to-digital converter survey and analysis," *IEEE Journal on Selected Areas in Communications*, vol. 17, no. 4, pp. 539–550, 1999.
- [11] Z. Cheng, S. Shi, Z. He, and B. Liao, "Transmit Sequence Design for Dual-Function Radar-Communication System With One-Bit DACs," *IEEE Transactions on Wireless Communications*, vol. 20, no. 9, pp. 5846–5860, Sep. 2021.
- [12] O. Dizdar, A. Kaushik, B. Clerckx, and C. Masouros, "Rate-Splitting Multiple Access for Joint Radar-Communications with Low-Resolution DACs," in *Proc. IEEE International Conference on Communications Workshops*, Montreal, QC, Canada, Jun. 2021, pp. 1–6.
- [13] H. Ruan and F. Liu, "Task-Based Quantizer Design for Sensing With Random Signals," Mar. 2024, arXiv:2403.11187. [Online]. Available: <http://arxiv.org/abs/2403.11187>
- [14] S. Zhu, F. Xi, S. Chen, and A. Nehorai, "A Low-Complexity MIMO Dual Function Radar Communication System via One-Bit Sampling," in *Proc. IEEE International Conference on Acoustics, Speech and Signal Processing (ICASSP)*, Toronto, ON, Canada, Jun. 2021, pp. 8223–8227.
- [15] D. Ma, N. Shlezinger, T. Huang, Y. Liu, and Y. C. Eldar, "Bit Constrained Communication Receivers In Joint Radar Communications Systems," in *Proc. IEEE International Conference on Acoustics, Speech and Signal Processing*, Toronto, ON, Canada, Jun. 2021, pp. 8243–8247.
- [16] Y. Luo, J. A. Zhang, X. Huang, W. Ni, and J. Pan, "Optimization and Quantization of Multibeam Beamforming Vector for Joint Communication and Radio Sensing," *IEEE Transactions on Communications*, vol. 67, no. 9, pp. 6468–6482, Sep. 2019.
- [17] D.-P. Xia, Y. Zhang, P. Cai, and L. Huang, "An Energy-Efficient Signal Detection Scheme for a Radar-Communication System Based on the Generalized Approximate Message-Passing Algorithm and Low-Precision Quantization," *IEEE Access*, vol. 7, pp. 29 065–29 075, 2019.
- [18] Z. Wu, Y.-F. Liu, W.-K. Chen, and C. Masouros, "Quantized Constant-Envelope Waveform Design for Massive MIMO DFRC Systems," Mar. 2024, arXiv:2403.06185. [Online]. Available: <http://arxiv.org/abs/2403.06185>
- [19] Q. Zhu, M. Li, R. Liu, and Q. Liu, "Cramér-Rao Bound Optimization for Active RIS-Empowered ISAC Systems," *IEEE Transactions on Wireless Communications*, pp. 1–1, 2024.
- [20] X. Wang, Z. Fei, J. Huang, and H. Yu, "Joint Waveform and Discrete Phase Shift Design for RIS-Assisted Integrated Sensing and Communication System Under Cramer-Rao Bound Constraint," *IEEE Transactions on Vehicular Technology*, vol. 71, no. 1, pp. 1004–1009, Jan. 2022.
- [21] P. Kumari, A. Mezghani, and R. W. Heath, "A Low-Resolution ADC Proof-of-Concept Development for a Fully-Digital Millimeter-wave Joint Communication-Radar," in *Proc. IEEE International Conference on Acoustics, Speech and Signal Processing (ICASSP)*, Barcelona, Spain, May 2020, pp. 8619–8623.
- [22] P. Kumari, K. U. Mazher, A. Mezghani, and R. W. Heath, "Low Resolution Sampling for Joint Millimeter-Wave MIMO Communication-Radar," in *Proc. IEEE Statistical Signal Processing Workshop (SSP)*, Fribourg im Breisgau, Germany, Jun. 2018, pp. 193–197.
- [23] C.-Y. Wu, T. Zhang, J. Li, and T. F. Wong, "Parameter Estimation in PMCW MIMO Radar Systems With Few-Bit Quantized Observations," *IEEE Transactions on Signal Processing*, vol. 70, pp. 810–821, 2022.
- [24] A. Chowdhury, A. Bazzi, and M. Chafii, "On Hybrid Radar Fusion for Integrated Sensing and Communication," *IEEE Transactions on Wireless Communications*, vol. 23, no. 8, pp. 8984–9000, 2024.
- [25] J. Liu, Z. Luo, and X. Xiong, "Low-Resolution ADCs for Wireless Communication: A Comprehensive Survey," *IEEE Access*, vol. 7, pp. 91 291–91 324, 2019.
- [26] J. Mo, P. Schniter, and R. W. Heath, "Channel Estimation in Broadband Millimeter Wave MIMO Systems With Few-Bit ADCs," *IEEE Transactions on Signal Processing*, vol. 66, no. 5, pp. 1141–1154, 2018.
- [27] A. Mezghani, F. Antreich, and J. A. Nossek, "Multiple parameter estimation with quantized channel output," in *2010 International ITG Workshop on Smart Antennas (WSA)*, 2010, pp. 143–150.
- [28] M. Stein, A. Mezghani, and J. A. Nossek, "A Lower Bound for the Fisher Information Measure," *IEEE Signal Processing Letters*, vol. 21, no. 7, pp. 796–799, Jul. 2014.
- [29] J. J. Bussgang, "Crosscorrelation functions of amplitude-distorted Gaussian signals," Massachusetts Institute Of Technology (MIT), Cambridge, Massachusetts, Tech. Rep. 216, Mar. 1952. [Online]. Available: <https://dspace.mit.edu/bitstream/handle/1721.1/4847/RLE-TR-216-14259781.pdf?sequence=1>
- [30] A. Mezghani and J. A. Nossek, "Capacity Lower Bound of MIMO Channels with Output Quantization and Correlated Noise," in *Proc. IEEE International Symposium on Information Theory*, 2012, pp. 1–5.
- [31] J. Max, "Quantizing for minimum distortion," *IEEE Transactions on Information Theory*, vol. 6, no. 1, pp. 7–12, Mar. 1960.
- [32] K. U. Mazher, A. Mezghani, and R. W. Heath, "Improved CRB for Millimeter-Wave Radar With 1-Bit ADCs," *IEEE Open Journal of Signal Processing*, vol. 2, pp. 318–335, 2021.
- [33] S. Diggavi and T. Cover, "The worst additive noise under a covariance constraint," *IEEE Transactions on Information Theory*, vol. 47, no. 7, pp. 3072–3081, Nov. 2001.
- [34] A. Papoulis and S. U. Pillai, *Probability, Random Variables, and Stochastic Processes*, 4th ed. New York, USA: McGraw-Hill, 2002.
- [35] B. Ma, H. Shah-Mansouri, and V. W. S. Wong, "Full-duplex relaying for d2d communication in millimeter wave-based 5g networks," *IEEE Transactions on Wireless Communications*, vol. 17, no. 7, pp. 4417–4431, 2018.
- [36] I. A. Hemadeh, K. Satyanarayana, M. El-Hajjar, and L. Hanzo, "Millimeter-wave communications: Physical channel models, design considerations, antenna constructions, and link-budget," *IEEE Communications Surveys & Tutorials*, vol. 20, no. 2, pp. 870–913, 2018.
- [37] B. Laporte-Fauret, G. Ferré, D. Dallet, B. Minger, and L. Fuché, "Adc resolution for simultaneous reception of two signals with high dynamic range," in *2018 25th IEEE International Conference on Electronics, Circuits and Systems (ICECS)*, 2018, pp. 729–732.